JOURNAL OF GEOPHYSICAL RESEARCH, VOL. 102, NO. D14, PAGES 16,971–16,988, JULY 27, 1997

Remote sensing of aerosol properties over oceans using the MODIS/EOS spectral radiances

D. Tanré,[1] Y. J. Kaufman,[2] M. Herman,[1] and S. Mattoo[3]

Abstract. Spectral radiances measured at the top of the atmosphere in a wide spectral range (0.55–2.13 μm) are used to monitor the aerosol optical thickness and the aerosol size distribution (integrated on the vertical column) of the ambient (undisturbed) aerosol over the oceans. Even for the moderate resolution imaging spectrometer (MODIS) wide spectral range, only three parameters that describe the aerosol loading and size distribution can be retrieved. These three parameters are not always unique. For instance, the spectral radiance of an aerosol with a bilognormal size distribution can be simulated very well with a single lognormal aerosol with an appropriate mean radius and width of distribution. Preassumptions on the general structure of the size distribution are therefore required in the inversion of MODIS data. The retrieval of the aerosol properties is performed using lookup table computations. The volume size distribution in the lookup table is described with two lognormal modes: a single mode to describe the accumulation mode particles (radius <0.5 μm) and a single coarse mode to describe dust and/or salt particles (radius >1.0 μm). Note that two accumulation modes may be present, one dominated by gas phase processes and a second dominated by cloud phase processes. The coarse mode can also be split into several partially overlapping modes describing maritime salt particles and dust. The aerosol parameters we expect to retrieve are η, the fractional contribution of the accumulation mode to scattering; τ, the spectral optical thickness; and r_m, the mean particle size of the dominant mode. Additional radiative quantities such as asymmetry parameter and effective radius are derived subsequently. The impact of the surface conditions, wind speed and chlorophyll content on the retrieval is estimated, the impact of potential sources of error like the calibration of the instrument is also tested. The algorithm has been applied successfully to actual data sets provided by the Thematic Mapper on Landsat 5 and by the MODIS airborne simulator on the ER-2 and tested against ground and airborne measurements. A first estimate of the general accuracy is $\Delta\tau = \pm 0.05 \pm 0.05\tau$ (at 550 nm), $\Delta r_m = 0.3 r_m$, $\Delta\eta = \pm 0.25$.

1. Introduction

Several core projects of the International Geosphere-Biosphere Program (IGBP-Global Change) are devoted to the role of aerosol particles: (1) aerosol is important in geochemical cycles, (2) it plays a role in tropospheric chemistry, and (3) it has to be considered in climate modeling because of its direct and indirect radiative effects. For a detailed review and illustrations of its potential impact, the reader is referred to the overview of this special issue [*Kaufman et al.*, this issue]. It is clear that understanding of the links between the different processes requires global coverage from satellite, but all the "key" aerosol parameters, optical, physical, and chemical properties, cannot be detected from space.

Since the detected radiation corresponds to solar light reflected simultaneously by the aerosol layer and by the Earth surface, the first step in deriving the aerosol properties is to correct the satellite signal for the surface contribution. Only then can the aerosol contribution to the detected radiance be related to the aerosol optical properties: the optical thickness (related to the aerosol content), the ratio between the scattering and the absorption efficiencies of the aerosol particles, the phase function, and the polarization ratio. These aerosol optical characteristics can be related to their physical/chemical properties (composition, refractive index, and size distribution) which can be described in mathematical terms using the Mie theory for spherical particles [*Van de Hulst*, 1957] or alternative theories for other shapes [*Wiscombe and Mugnai*, 1988; *Koepke and Hess*, 1988; *Mishchenko and Travis*, 1994; *Mishchenko et al.*, 1995].

With new sensor capabilities, POLDER [*Deschamps et al.*, 1994] on ADEOS 1 launched in August 1996, MODIS [*Salomonson et al.*, 1989] and MISR [*Diner et al.*, 1989] on EOS AM 1 scheduled in June 1998, and EOSP [*Travis*, 1993] on EOS AM 2 scheduled in 2004, more information using the solar-reflected radiances will be available. The spectral signature over a wide spectral range [*King et al.*, 1992], the angular dependence [*Martonchick and Diner*, 1992], and the polarization characteristics [*Deuzé et al.*, 1993] of the surface-atmosphere system will be measured. Here we are concerned with the use of MODIS spectral radiances measured over a dark ocean surface. The aerosol quantities which can be derived from the current satellites are very restricted due to the limited number of available channels, one channel for GOES

[1]Laboratoire d'Optique Atmosphérique, Université des Sciences et Technologies de Lille, Villeneuve d'Ascq, France.
[2]Laboratory for Atmospheres, NASA Goddard Space Flight Center, Greenbelt, Maryland.
[3]Applied Research Corporation, Landover, Maryland.

Paper number 96JD03437.
0148-0227/97/96JD-03437$09.00

Table 1a. Characteristics of the MODIS Channels Used for the Aerosol Retrieval Over Ocean

Center Wavelength	$Ne\Delta L$	$Ne\Delta\rho$	Maximum Reflectance	SNR	Pixel Size at Nadir, m
470	0.145	2.35×10^{-4}	0.96	243	500
555	0.127	2.11×10^{-4}	0.86	228	500
659	0.170	3.39×10^{-4}	1.38	128	250
865	0.123	3.99×10^{-4}	0.92	201	250
1240	0.073	5.06×10^{-4}	0.47	74	500
1640	0.027	3.63×10^{-4}	0.94	275	500
2130	0.009	3.06×10^{-4}	0.75	110	500

MODIS, moderate resolution imaging spectrometer. $Ne\Delta\rho$ corresponds to a Sun at zenith ($\theta_s = 0°$). SNR, signal to noise ratio.

or Meteosat and two channels for AVHRR/NOAA; for example, see *Fraser* [1976], *Mekler et al.* [1977], *Carlson* [1979], *Griggs* [1979], *Koepke and Quenzel* [1979], *Norton et al.* [1980], *Durkee* [1985], *Rao et al.* [1989], *Kaufman et al.* [1990], *Dulac et al.* [1992] and *Jankowiak and Tanré* [1992]. Typically, these algorithms can derive only the total aerosol content assuming an aerosol model representative of the local conditions. With the MODIS instrument we first expected to retrieve aerosol size distribution from the spectral signature of the radiances, between 0.415 and 2.2 μm, using an approach developed by *King et al.* [1978] but for the spectral signature of the optical thickness measurements. However, a recent sensitivity study [*Tanré et al.*, 1996] showed the limitation of the retrieval using the satellite radiance. Because of possible compensation between the spectral dependence of the phase function and that of the optical thickness, the radiance which is the product of both can be spectrally independent. Note also that narrow width of the lognormal distribution of an accumulation mode can cause an erratic spectral dependence of $L(\lambda)$ as shown by *Kaufman et al.* [1990] for AVHRR and by *Tanré et al.* [1996] for MODIS. Since sensitivity of the spectral reflected radiances to details of the aerosol size distribution may be low and because of lack of uniqueness of the general solution, we changed our philosophy regarding the retrieval scheme. Instead of deriving the actual aerosol size distribution, in addition to the aerosol spectral optical thickness and loading, we plan to derive (1) η, the fractional contribution of the accumulation mode to scattering, and (2) the specific size of the dominant aerosol mode.

We present in this paper our strategy for inversion of the MODIS spectral data as well as some preliminary results obtained from existing data sets. Section 2 recalls the MODIS characteristics. The strategy is explained in section 3, the algorithm is described in section 4 and the sensitivity study in section 5. In section 6 the algorithm is applied to Thematic Mapper (TM) data on Landsat 5, which has similar spectral bands to MODIS and to the MODIS airborne simulator on the ER-2. Discussion of some issues, like the cloud screening, the stratospheric correction, or the uniformity of the aerosol layer is given in section 7.

2. Characteristics of the MODIS Instrument

The moderate resolution imaging spectrometer (MODIS) instrument is designed to fly on the EOS (Earth Orbiting System) morning and afternoon platforms, with daily global coverage. It is dedicated to perform measurements in the solar spectrum and the infrared regions from 0.415 to 14.235 μm [*Salomonson et al.*, 1989]. The characteristics of the seven spectral bands which are potentially useful for the remote sensing of aerosols are reported in Table 1a. The spectral domain of interest is covered by three of the four focal planes, the visible (VIS) from 0.412 to 0.551 μm, the near infrared (NIR) from 0.650 to 0.940 μm, and the short-wavelength/medium-wavelength infrared (SWIR/MWIR) from 1.240 to 4.565 μm. The spectral stability is expected to be better than 2 nm and the instantaneous field of view varies between 250 and 500 m. The noise equivalent differential spectral radiance ($Ne\Delta L$ in W/m^2/μm/sr) is also reported as well as the $Ne\Delta\rho$ computed from

$$Ne\Delta\rho = Ne\Delta L \frac{\pi}{F_0 \cos(\theta_s)} \quad (1)$$

where F_0 is the extraterrestrial solar irradiance and $\theta_s = \text{Arcos}(\mu_s)$ is the solar zenith angle. In Table 1a, $Ne\Delta\rho$ is given for a Sun at zenith ($\theta_s = 0°$).

Because the aerosol loading is usually expressed by the aerosol optical thickness instead of reflectance or radiance values, we computed the corresponding $Ne\Delta\tau$ using the single-scattering approximation,

$$Ne\Delta\tau = Ne\Delta\rho \frac{4\mu_v\mu_s}{\omega_0 P(\Theta)} = \frac{\pi Ne\Delta L}{F_0} \frac{4\mu_v}{\omega_0 P(\Theta)} \quad (2)$$

The $Ne\Delta\tau$ reported in Table 1b is estimated in the most unfavorable conditions, i.e., in the 2.13 μm channel where the optical thickness is expected to be minimum. Two cases are selected, pure maritime conditions and presence of Saharan dust. Again conservative conditions are selected, i.e., a nadir observation ($\mu_v = 1$) and the lowest value of the phase function obtained for a scattering angle around 120°. Following *Shettle and Fenn* [1979], a value of 0.05 is considered for the phase function of the dust-like model, while for maritime conditions the phase function is slightly larger, around 0.08. The result is a noise equivalent differential spectral thickness of 2.4×10^{-2} for Saharan dust and of 1.5×10^{-2} for maritime conditions (Table 1b). As the aerosol product is not given on a pixel by pixel basis (0.5×0.5 km^2) but rather over a grid, we consider two grid sizes, 10×10 km^2 or 50×50 km^2 to divide the noise by a factor 20 and 100, respectively. From *Hoppel et al.* [1990], who reports Ångström parameters for very clean air, the expected optical thickness, τ^{st}, in the 2.13 μm channel, would be around 0.01 for maritime aerosols, while for dust, a minimum value of 0.05 can be assumed [*Tanré et al.*, 1988b]. The signal to noise ratio (SNR) defined by $\tau^{st}/Ne\Delta\tau$ is reported in Table 1b. Let us emphasize that the values are slightly overestimated because it is unlikely that all pixels in an area will be cloud free. Since the global cloud cover is about 0.6, the number of useful pixels is reduced by a factor of 0.4 and SNR goes down by about a factor of 0.63. The aerosol product will be delivered over a grid of 10×10 km^2 but will be

Table 1b. Aerosol Optical Thickness Sensitivity at 2.13 μm Resulting From Radiometric Noise

Grid Size, km^2	$Ne\Delta\tau$ (Dust)	SNR	$Ne\Delta\tau$ (Maritime)	SNR
0.5×0.5	2.4×10^{-2}	2.0	1.5×10^{-2}	0.66
10×10	1.2×10^{-3}	42	0.8×10^{-3}	13
50×50	2.4×10^{-4}	208	1.5×10^{-4}	66

Dust and maritime conditions are considered.

also gridded on a 1° × 1° grid, thus increasing the SNR in clean conditions.

3. Strategy

Our strategy is based on a lookup table (LUT) approach; that is, radiative transfer calculations are precomputed for several values of the aerosol and surface parameters. The measured spectral radiances are compared with the LUT radiances until the best "fit" is obtained. This best fit, or several of the best fits, is the answer of the inversion. The input parameters, aerosol models, and surface conditions, needed for performing the computations, are hereinafter described.

3.1. Aerosol Models

Aerosols are formed through two main processes, a primary source which includes dispersion of material from the Earth's surface (like soil dust, sea-salt particles, biomass burning, industrial debris) and a secondary source resulting from atmospheric chemical reactions or condensation or coagulation processes (the reader is referred to *Mészáros* [1981] and *Hidy* [1984] books for more details). There are several classifications of atmospheric aerosols, but the most widely used is according to their size. *Whitby* [1978] showed that an actual size distribution can be expressed by a sum of lognormal functions, each representing a different physical or chemical process. He suggests three modes, a nuclei mode, generated by spontaneous nucleation of the gaseous material for particles less than 0.04 μm diameter, the accumulation mode for particles between 0.04 and 0.5 μm diameter resulting from coagulation and in cloud processes [*Hoppel et al.*, 1990], and the coarse mode with particles larger than 1.0 μm diameter for aerosols originating from the Earth's surface (land and ocean). The classification is quite similar to the *Junge*'s [1963] designation who refers to Aitken, large and giant particles.

The use of the lognormal functions for tropospheric aerosol size distribution was also suggested by *Shettle and Fenn* [1979], *d'Almeida* [1987], *Kaufman et al.* [1994], and *Kaufman and Holben* [1996]. Therefore we can assume that aerosol size distributions follow a lognormal distribution, or a sum of several, defined by

$$n(r) = \frac{dN(r)}{dr} = \frac{N}{(2\pi)^{1/2}\sigma 2.3r}\exp\left\{-\frac{(\log r - \log r_m)^2}{2\sigma^2}\right\} \quad (3)$$

where N is the density number, r_m is the median radius, and σ is the standard deviation of log r; that is, $\sigma^2 = \langle(\log r - \log r_m)^2\rangle$.

We shall assume that after correction for stratospheric aerosol, the tropospheric aerosol model is described by a bimodal distribution, i.e., a sum of 2 lognormals,

Table 2a. Parameters of Lognormal Size Distribution for Small Mode

Aerosol Model	Median Radius r_m^s	s.d., σ^s	Refractive Index
S_A	0.02	0.60	1.45–0.0035i
S_B	0.04	0.60	1.45–0.0035i
S_C	0.04	0.40	1.45–0.0035i
S_D	0.08	0.60	1.40–0.0035i
S_E	0.08	0.40	1.40–0.0035i

Table 2b. Parameters of Lognormal Size Distribution for Large Mode

Aerosol Model	Median Radius r_m^l	s.d., σ^l	Refractive Index
L_A	0.40	0.60	1.40–0.0035i
L_B	0.60	0.40	1.40–0.0035i
L_C	0.60	0.60	1.45–0.0035i
L_D	0.60	0.80	1.45–0.0035i
L_E	1.00	0.60	1.50–0.0035i
L_F	1.00	0.80	1.50–0.0035i

$$n(r) = \frac{dN(r)}{dr} = \sum_{j=1}^{2}\frac{dN_j(r)}{dr} \quad (4)$$

where $(dNj(r)/dr)$ expressed in terms of natural logarithm is given by

$$\frac{dN_j(r)}{dr} = \frac{N_j}{(2\pi)^{1/2}\sigma 2.3r}\exp\left\{-\frac{1}{2\sigma^2}\left(\frac{\ln r - \ln r_m}{\ln (10)}\right)^2\right\} \quad (5)$$

The nuclei mode is not considered since it corresponds to particles that are too small to be detected from the scattered light.

The parameters σ, r_m of each mode in (5), called hereinafter small (S) and large (L) modes are reported in Tables 2a and 2b, i.e., the median radius, the standard deviation (natural logarithm), and the refractive index. The small mode merges the contribution to the accumulation mode that is dominated by gas phase processes with that by cloud phase processes. The large mode merges maritime particles with dust. The selected aerosol models are derived mainly from ground-based sampling of the aerosol characteristics, and they may not fully represent the optical properties of the ambient aerosol integrated on the vertical column. In order to avoid this difficulty there is a need to measure the climatology and variability of the size distribution and scattering phase function of the ambient undisturbed aerosol, integrated on the vertical column. A network of Sun/sky radiometers is being developed and implemented to perform such measurements [*Holben et al.*, 1996]. The optical data collected by such instruments (for example, of measurements and analysis, see *Nakajima et al.* [1983] and *Kaufman et al.* [1994]) will be used to test and modify the present aerosol models.

3.2. Physical Processes

The satellite signal is composed from two contributions, atmospheric radiative processes and surface reflection. The radiative code developed by *Ahmad and Fraser* [1982] is used in the computations. It accounts for multiple scattering in the atmosphere by molecules and aerosol particles and for reflection of the light by the surface. It also includes polarization effects. Over the ocean the surface reflection includes three contributions: the Fresnel reflection on the waves called "glitter," the lambertian reflectance coming from underwater scattering elements (sediments, pigments, etc.), and reflection by foam.

The Fresnel reflection on the sea surface is calculated using the rough ocean model proposed by *Cox and Munk* [1954]. They give the probability distribution of surface slopes as a function of the wind speed and direction. In our computations, we selected the simple case of an ocean independent on the

Table 3a. Optical Properties and Effective Radius of Size Distribution for Small Modes

Aerosol Model	Effective Radius	Single-Scattering Albedo	Asymmetry Factor	Backscattering Ratio
S_A	0.05	0.932	0.367	0.360
S_B	0.10	0.969	0.588	0.270
S_C	0.06	0.920	0.269	0.398
S_D	0.20	0.976	0.720	0.210
S_E	0.12	0.967	0.567	0.280

Optical properties are given at 550 nm.

wind direction. The specular reflection of the light by waves is given by the classical fresnel equations. Because the glitter contribution is several orders of magnitude larger than the aerosol contribution, we will avoid pixels which are close to the specular direction (i.e., ±30° around the solar zenith angle and ±30° around the solar azimuth angle); efforts are under way to better define the glint mask. Even far from the specular direction, the sea surface contributes through the Fresnel reflection of the diffuse skylight.

The percentage of the sea covered by foam depends on the wind speed following *Koepke*'s [1984] model. According to *Payne* [1972] the reflectance of the foam is assumed lambertian. In the visible and near-infrared parts of the spectrum the reflectance of the foam is assumed independent of the wavelength. It is also assumed that the reflectance in the SWIR comparing with the visible/NIR reflectance decreases by a factor of 0.8, 0.5, and 0.25 at 1240, 1640, and 2130 nm, respectively [*Whitlock et al.*, 1982]. Recent measurements [*Frouin et al.*, 1996] show that this spectral dependence is questionable, even in the NIR at 865 nm, and may result in additional uncertainties.

The water-leaving radiance depends on turbidity and pigment concentrations. Waters with high chlorophyll contents (called case 1 by *Morel and Prieur* [1977]) show large variations of the reflectance at 470 nm relative to the pigment concentrations. Reflectance at 555 nm may be also affected for pigment concentrations larger than 0.5 mg/m^3 [*Gordon*, this issue], but reflectances are quite stable in the other bands. Case 1 is representative of open ocean conditions. The band at 659 nm can be affected by chlorophyll *a* fluorescence, but the resulting error is negligible [*Gordon*, 1979]. On the other hand, waters with higher concentrations of inorganic particles relative to phytoplankton (called case 2) show large variation in the 470, 555, and 659 nm channels, and the resulting uncertainty in the surface reflectance values is large. They are usually representative of coastal zones, and the retrieved aerosol parameters can be flagged as less reliable in these regions.

3.3. Description of the Lookup Table (LUT)

We generated a lookup table of the radiance detected in the MODIS spectral bands for each aerosol size mode, the small particle mode (five cases) describing the accumulation mode particles, and the large particle mode (six cases) describing the coarse particles. Radiative properties are reported in Tables 3a and 3b, respectively.

Several values of aerosol total loading are considered for each mode and described by the optical thickness τ at 0.55 μm. Extreme conditions are included in the LUT, a pure molecular atmosphere ($\tau_a = 0.0$) and a very turbid atmosphere ($\tau_a = 2.0$) as observed during dust events [*Tanré et al.*, 1988b] or in smoke plumes generated from biomass burning [*Holben et al.*, 1991]. Three intermediate values are considered ($\tau_a = 0.2$, 0.5, 1.0), a linear interpolation between them (or a more sophisticated method) is then applied. Computations are performed for 15 zenith view angles ($\theta_v = 0°$ to 84 by step of 6°) and 46 azimuth angles ($\phi_v = 0°$ to 180° by step of 4°); one Sun incident angle has been presently considered, $\theta_s = 36°$ and $\phi_s = 0°$. Additional solar incident angles will be used in the final algorithm.

The existing computations have been performed for wind speed of 7.0 m/s and a zero water-leaving radiance in all the channels. We shall build additional LUT for other wind speeds and for different chlorophyll concentrations; the most appropriate LUT will be selected from the wind speed made available to Mission to Planet Earth Program by the Laboratory for Atmospheres Data Assimilation Office (DAO) at Goddard Space Flight Center (GSFC) [*Schubert et al.*, 1993] and from the chlorophyll content derived from other MODIS channels [*Gordon*, this issue].

4. Description of the Algorithm

Our approach to generate the LUT and to use them is based on the recent simplification suggested by *Wang and Gordon* [1994] that the multiple-scattering radiance from two lognormals can be approximated by the weighted average of the radiances of the individual modes, calculated for the same optical thickness. When the two modes have different absorbing properties, difficulties are encountered [*Kahn et al.*, this issue], but we decided to adopt this approximation in the present study because the condition of application is generally achieved. The advantage of this important simplification is that the LUT has now only 11 aerosol models (5 small and 6 large) instead of 281 combinations, assuming, for instance, 11 relative concentrations between the two modes (281 = 5 ($\eta = 0$) + 6 ($\eta = 1$) + 5 × 6 × 9 (η = 1 to 9)). The input of the algorithm is the averaged cloud-free MODIS measurements in the seven solar bands over a box of 10 × 10 km^2 or of 50 × 50 km^2 (the cloud screening and the data processing for handling the possible nonuniformity of the aerosol layer, type, and content within the box are not discussed here).

4.1. Principle

The total radiance, L^c_λ, at the satellite level is written

$$L^c_\lambda(\mu_s, \mu_v, \phi_v) = \eta L^s_\lambda(\mu_s, \mu_v, \phi_v) + (1 - \eta) L^l_\lambda(\mu_s, \mu_v, \phi_v) \quad (6)$$

where $L^s_\lambda(\mu_s, \mu_v, \phi_v)$ and $L^l_\lambda(\mu_s, \mu_v, \phi_v)$ are the radiances of the small (S) and large (L) modes, respectively. Equation (6) assumes that the effect of multiple scattering on the spec-

Table 3b. Optical Properties and Effective Radius of Size Distribution for Large Modes

Aerosol Model	Effective Radius	Single-Scattering Albedo	Asymmetry Factor	Backscattering Ratio
L_A	0.98	0.938	0.764	0.172
L_B	0.89	0.939	0.744	0.181
L_C	1.48	0.905	0.763	0.167
L_D	2.97	0.856	0.805	0.142
L_E	2.46	0.857	0.799	0.144
L_F	4.95	0.810	0.828	0.125

Optical properties are given at 550 nm.

Table 4a. Optical Properties and Effective Radius of Input Data Sets Included in Lookup Table

Case	Small Mode	r^s_{eff}	Large Mode	r^l_{eff}	r_{eff}	Ratio η	Optical Thickness τ	Asymmetry Factor g
0	...	...	...	...	...	...	0.000	...
1	S_A	0.049	...	...	0.049	1.00	0.200	0.367
2	S_A	0.049	...	...	0.049	1.00	0.500	0.367
3	S_A	0.049	...	...	0.049	1.00	1.000	0.367
4	S_A	0.049	...	...	0.049	1.00	2.000	0.367
5	S_B	0.098	...	...	0.098	1.00	0.500	0.588
6	...	...	L_A	0.984	0.984	0.00	0.200	0.764
7	...	...	L_A	0.984	0.984	0.00	0.500	0.764
8	...	...	L_A	0.984	0.984	0.00	1.000	0.764
9	...	...	L_A	0.984	0.984	0.00	2.000	0.764
10	S_A	0.049	L_A	0.984	0.077	0.41	0.200	0.573
11	S_A	0.049	L_A	0.984	0.077	0.41	0.500	0.573

Optical properties are given at 550 nm.

tral radiance is independent on the size distribution. The objective is to retrieve the ratio η and the small and large modes of the size distribution which give the best fit between the measurements and the LUT computations. The total aerosol optical thickness and the optical thicknesses of each mode at 550 nm is also derived.

The selection of the aerosol models is performed by minimizing the following quantity ε_{sl}:

$$\varepsilon_{sl,i} = \sqrt{\frac{1}{n}\sum_{k=1}^{n}\left(\frac{L_k^m(\mu_s, \mu_v, \phi_v) - L_k^c(\mu_s, \mu_v, \phi_v)}{L_k^m(\mu_s, \mu_v, \phi_v) + 0.01}\right)^2} \quad (7)$$

where $L_k^m(\mu_s, \mu_v, \phi_v)$ and $L_k^c(\mu_s, \mu_v, \phi_v)$ are the measured and the computed radiances in channel k, and i is the combination index ($i = 1, 5 \times 6$). The radiances are normalized to reflectance units. For clean conditions with strong spectral dependence, $L^m_{2130}(\mu_s, \mu_v, \phi_v)$ is close to 0.0 with high uncertainty in its relative value. The constant "0.01" in (7) minimizes this uncertainty on the retrieval; a sensitivity study showed that its exact value is not critical. In the shortest channel (470 nm) the surface contribution is very uncertain if information on the ocean color is not available. As it may result in errors in the estimate of the aerosol contribution, it will be ignored in the retrieval algorithm, and the summation term n in (7) is equal to 6.

4.2. Method

For the five small particle modes and the six large modes the radiances $L^S_\lambda(\mu_s, \mu_v, \phi_v)$ and $L^l_\lambda(\mu_s, \mu_v, \phi_v)$ are in the LUT for the five values of the aerosol optical thickness τ_a at 550 nm (0.0, 0.2, 0.5, 1.0, and 2.0) and for the geometrical conditions corresponding to the observations. As already mentioned, the surface conditions of the LUT, wind speed, and chlorophyll content are selected from ancillary data. Given one of the 30 possible combinations of small (S) and large (L) modes, for any value of η, we can compute the total radiance $L^C_{550}(\mu_s, \mu_v, \phi_v)$ from (6) for each of the five values of the optical thickness. The optical thickness is derived from the radiance at 550 nm by linear interpolation for the considered combination. For each mode the optical thickness is derived in the five other channels, and the satellite radiances are computed using (6) in order to obtain the quantity ε_{sl} defined in (7). In this retrieval process, the combination that gives the smallest residual error $\varepsilon_{sl}(\eta)$ for the best selected value of η is called the best solution. We also provide the aerosol parameters averaged over the models i which gives $\varepsilon_{sl,i} < 3\%$; it is called average solution, and the standard deviation is also provided.

4.3. By-products

Simultaneously to the computation of the ratio between the modes η, the effective radius of the dominant mode, and the spectral optical thickness τ_a, associated parameters are also computed in the LUT; they correspond to quantities which govern the radiative transfer computations and aerosol direct forcing (asymmetry factor and backscattering ratio) and to physical properties like the number of particles, the cloud condensation nuclei (CCN) number, or the moments of the size distribution. We do not derive the single-scattering albedo since we showed in a previous study [*Tanré et al.*, 1996] that the spectral dependence of the radiance is independent of the real and imaginary parts of the refractive index, while the aerosol effective radius should be accurately determined, even if the actual size distribution does not follow a simple lognormal law [*Hansen and Hovenier*, 1974], the other physical parameters like the mass or the CCN number depend on the exact shape of the size distribution. Since they are not reliable at this stage, they are not delivered as products but are rather considered as research tools. Nevertheless, they are very interesting to retrieve on a global scale. Further studies will show for which aerosol types and for what conditions these additional parameters are representative.

Let us mention that the derivation of these products needs additional computations since the weight used to combine the radiances is not the same weight that is used to combine the aerosol modes. So, the optical thicknesses of the small and large modes are first retrieved, then the asymmetry parameter and the backscattering ratio are computed from equations (A2) and (A4) reported in the Appendix. The number of particles per cubic meter of each mode, N^s and N^l, are also derived from the ratio between the optical thicknesses and the extinction coefficients; next the moments of the size distribution (volume and effective radius mainly) and the number of CCN are computed from (A6) to (A8).

5. Sensitivity Study

We have tested the algorithm by applying it to (1) data sets which are included in the LUT and (2) data sets where the

Table 4b. Optical Properties and Effective Radius of Input Data Sets Not Included in Lookup Table

Case	Small Mode	r^s_{eff}	Large Mode	r^l_{eff}	r_{eff}	Ratio η	Optical Thickness τ	Asymmetry Factor g	Additional Variable
12	S_B	0.098	...	...	0.098	1.00	0.350	0.588	$\tau_a \neq$
13	S_B	0.098	...	...	0.098	1.00	0.850	0.588	$\tau_a \neq$
14	...	...	L_B	0.890	0.890	0.00	0.350	0.744	$\tau_a \neq$
15	...	...	L_B	0.890	0.890	0.00	0.850	0.744	$\tau_a \neq$
16	S_B	0.098	L_B	0.890	0.380	0.15	0.350	0.706	$\tau_a \neq$
17	S_B	0.098	L_B	0.890	0.380	0.15	0.850	0.706	$\tau_a \neq$
18	S_B	0.098	L_B	0.890	0.130	0.70	0.850	0.620	$\tau_a \neq$
19	S_A	0.049	...	...	0.049	1.00	0.200	0.367	$v = 5\ \text{m s}^{-1}$
20	...	...	L_A	0.984	0.984	0.00	0.200	0.764	$v = 5\ \text{m s}^{-1}$
21	S_A	0.049	L_A	0.984	0.077	0.41	0.200	0.572	$v = 5\ \text{m s}^{-1}$
22	S_A	0.049	...	...	0.049	1.00	0.200	0.367	$m = 1.50$
23	...	...	L_D	2.970	2.970	0.00	0.200	0.805	$m = 1.50$
24	S_A	0.049	L_D	2.970	0.395	0.15	0.200	0.711	$m = 1.50$
25	S_A	0.049	L_D	2.970	0.086	0.70	0.200	0.481	$m = 1.50$

Optical properties are given at 550 nm.

value of one of the parameters, for example, optical thickness, wind speed, or refractive index, is not included in the LUT. In addition, we have performed simulations for considering issues like sensor calibration, contamination by glint, and wrong estimate of the water-leaving radiance. Results of the sensitivity study are provided for the following aerosol products: (1) the optical thickness τ_a at 550 nm, (2) the ratio η between the contributions to the radiance of the two modes, (3) the effective radius of the complete size distribution r_{eff}, and (4) the asymmetry parameter g at 550 nm.

We also discuss the accuracy of the retrieval of the median radius and of the standard deviation of the two modes in the simple case where there is no additional error.

5.1. Description of Input Data Sets

Table 4a describes sensitivity study cases for which the input is included in the LUT (cases 0–11). For the case of a single mode we selected two small modes S_A and S_B (see Table 2a) and one large mode L_A (see Table 2b); several optical thicknesses are considered, 0.0, 0.2, 0.5, 1.0, and 2.0. A mixing of the modes S_A and L_A with $\eta = 0.41$ have been performed for two values of the optical thickness, $\tau_a = 0.20$ and 0.50.

Table 4b summarizes the data sets where parameters are not included in the LUT. For several combinations of the small mode S_B and the large mode L_B we check the impact of the aerosol optical thickness with two additional values of τ_a, 0.35 and 0.85 (cases 12–18). Single modes, small mode S_B (cases 12 and 13) and large mode L_B (cases 14 and 15), double mode mixing S_B and L_B (cases 16–19), with $\eta = 0.15$ and 0.70, are considered. The impact of the wind speed is checked by using additional simulations with a wind speed of 5.0 m s^{-1} instead of 7.0 m s^{-1} for several aerosol models: single modes with S_A (case 19) and L_A (case 20) and a double mode mixing S_A and L_A with $\eta = 0.41$ (case 21). Since the errors affecting the radiances have a greater impact on derived quantities when the aerosol contribution is small, the smallest value of the optical thickness ($\tau_a = 0.20$) has been selected. The impact of the refractive index is tested. In cases 22 to 25, simulations are performed with a refractive index $m = 1.50$ and inverted with $m = 1.45$ for single modes, S_A and L_D, and also for a two-mode size distribution mixing S_A and L_D with $\eta = 0.15$ and 0.70. Again the smallest value of the optical thickness has been selected in the simulation since multiple scattering which occurs for large τ_a is expected to smooth the impact of the actual phase function.

5.2. Results With no Additional Errors

We first consider perfectly measured radiances; that is, there are no calibration errors, and there is no uncertainty in the surface reflectance, except due to error in the wind speed. For the four quantities τ_a, η, r_{eff} and g we adopt a scatter diagram plotting the retrieved values as a function of the input values (Figure 1). In quarter a, we report results obtained with inputs that are already included in the LUT, i.e., 11 cases (cases 1–11); in quarter b, we consider the 7 cases (cases 12–18) where the optical thickness values are not included in the LUT; in quarter c, the impact of the wind speed is considered (cases 19–21); and finally, we assess the effect of the refractive index

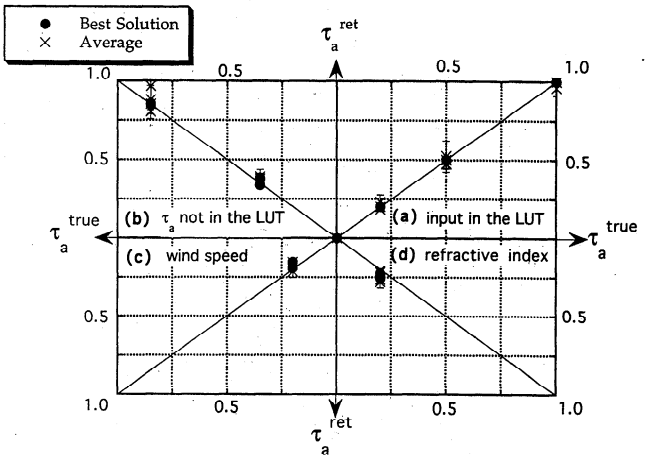

Figure 1. Scatter diagram of the optical thickness; the x axis corresponds to the input and the y axis to the retrieved values. Each quarter is devoted to a specific sensitivity study. Quarter a corresponds to an inversion where all the input are included in the lookup table (LUT). Quarter b corresponds to an inversion with values of the optical thickness not included in the LUT. Quarter c corresponds to a different wind speed. Quarter d corresponds to a different refractive index. The black dots correspond to the "best" model and the crosses to the "average" solution (see text). Error bars correspond to the standard deviation of the "average" solution.

Table 5a. Input and Retrieved Characteristics of Aerosol Models for "Best" Retrieval With All Parameters Included in LUT

	Input Values				Retrieved Values			
Case	Median Radius r_m^s	s.d. σ^s	Median Radius r_m^l	s.d. σ^l	Median Radius r_m^s	s.d. σ^s	Median Radius r_m^l	s.d. σ^l
1	0.02	0.60	...	...	0.02	0.60	...	...
2	0.02	0.60	...	...	0.02	0.60	...	...
3	0.02	0.60	...	...	0.02	0.60	...	...
4	0.02	0.60	...	...	0.02	0.60	...	...
5	0.04	0.60	...	...	0.04	0.60	...	...
6	...	...	0.40	0.60	...	...	0.40	0.60
7	...	...	0.40	0.60	...	...	0.40	0.60
8	...	...	0.40	0.60	...	...	0.40	0.60
9	...	...	0.40	0.60	...	...	0.40	0.60
10	0.02	0.60	0.40	0.60	0.02	0.60	0.40	0.60
11	0.02	0.60	0.40	0.60	0.02	0.60	0.40	0.60

in quarter d (cases 22–25). The black dots correspond to the "best" model and the crosses to the "average" solution as defined in section 4.2; the standard deviation of the "average" solution is given if appropriate. The median radius and the standard deviation of the modes are reported in Tables 5a and 5b for the "best" solution and in Tables 6a and 6b for the "average" solution.

5.2.1. Optical thickness τ_a. Note in Figure 1 the very good agreement for the "best" solution (black dots). The average solutions (crosses) may lead to slightly different values, but the general feature is that the optical thickness is retrieved with a very good accuracy, even when uncertainties in the refractive index and wind speed are introduced. Cases for τ_a = 2.0 (cases 4 and 9) are perfectly retrieved but are not reported in the plot, in order to keep a high resolution of the display results.

5.2.2. Ratio η. Similar positive conclusions can be made for the ratio η in Figure 2 when only the "best" solutions (black dots) are considered. On the other hand, large variations are observed in the "average" solutions (crosses) for double modes; that is, when $\eta \neq 0.0$ and 1.0. Because of the lack of uniqueness in the relationship between physical and optical properties [*Tanré et al.*, 1996], large fluctuations in the retrieved physical properties may occur, as already noticed in Tables 6a and 6b, and as a result, the algorithm has to compensate for them by selecting a wrong ratio η. It is interesting to notice that the standard deviation (error bars) is a good measure of the quality of the retrieval; when it is small, the "average" and "best" values are similar and quite close to the expected value.

5.2.3. Effective radius r_{eff}. Results for the effective radius r_{eff} are reported in Figure 3. Because of scale problem, Figure 3b is an enhancement of Figure 3a and roughly corresponds to the accumulation mode with values of r_{eff} smaller than 0.40. For the accumulation mode (Figure 3b), for single or double modes, the "best" effective radius (black dots) is well retrieved, while the "average" solution (crosses) can be far from the input value. These cases correspond to mixed mode. Again the standard deviation is a good indicator of the quality of the retrieval. For larger particles (Figure 3a) the retrieval is very well performed in quarters a, b, and, to a lesser extent, in quarter c. However, if uncertainty in the refractive index is considered, large errors result for both "best" and "average" solutions in quarter d. This is because the sensitivity of the spectral dependence is very weak for large particles, and a small uncertainty in this aerosol property has a large impact. Although the exact characteristics of the coarse mode are difficult to assess, it is

Table 5b. Input and Retrieved Characteristics of Aerosol Models for "Best" Retrieval With Parameters Not Included in LUT

	Input Values				Retrieved Values			
Case	Median Radius r_m^s	s.d. σ^s	Median Radius r_m^l	s.d. σ^l	Median Radius r_m^s	s.d. σ^s	Median Radius r_m^l	s.d. σ^l
12	0.04	0.60	...	...	0.08	0.40	...	...
13	0.04	0.60	...	...	0.04	0.60	...	...
14	...	...	0.60	0.40	...	...	0.60	0.40
15	...	...	0.60	0.40	...	...	0.60	0.40
16	0.04	0.60	0.60	0.40	0.08	0.40	0.60	0.40
17	0.04	0.60	0.60	0.40	0.04	0.60	0.60	0.40
18	0.04	0.60	0.60	0.40	0.04	0.60	0.40	0.60
19	0.02	0.60	...	...	0.04	0.40		
20	...	...	0.40	0.60	...	...	0.40	0.60
21	0.02	0.60	0.40	0.60	0.04	0.40	0.60	0.40
22	0.02	0.60	...	...	0.02	0.60	...	...
23	...	...	0.60	0.80	...	...	0.60	0.80
24	0.02	0.60	0.60	0.80	0.04	0.40	0.60	0.80
25	0.02	0.60	0.60	0.80	0.02	0.60	0.60	0.80

Table 6a. Input and Retrieved Characteristics of Aerosol Models for "Average" Retrieval With All Parameters Included in LUT

	Input Values				Retrieved Values			
Case	Median Radius r_m^s	s.d. σ^s	Median Radius r_m^l	s.d. σ^l	Median Radius r_m^s	s.d. σ^s	Median Radius r_m^l	s.d. σ^l
1	0.02	0.60	...	...	0.03 ± 0.01	0.47 ± 0.10	...	...
2	0.02	0.60	...	...	0.03 ± 0.01	0.52 ± 0.10	...	...
3	0.02	0.60	...	...	0.03 ± 0.01	0.52 ± 0.10	...	...
4	0.02	0.60	...	...	0.03 ± 0.01	0.52 ± 0.10	...	...
5	0.04	0.60	...	...	0.06 ± 0.02	0.50 ± 0.10	...	...
6	...	...	0.40	0.60	...	...	0.40 ± 0.02	0.60 ± 0.11
7	...	...	0.40	0.60	...	...	0.40 ± 0.02	0.60 ± 0.11
8	...	...	0.40	0.60	...	...	0.40 ± 0.02	0.60 ± 0.11
9	...	...	0.40	0.60	...	...	0.40 ± 0.02	0.60 ± 0.11
10	0.02	0.60	0.40	0.60	0.06 ± 0.02	0.51 ± 0.10	0.67 ± 0.23	0.62 ± 0.14
11	0.02	0.60	0.40	0.60	0.05 ± 0.02	0.47 ± 0.10	0.58 ± 0.19	0.60 ± 0.14

very important to notice that the algorithm is able to detect the presence of such large particles.

5.2.4. Asymmetry parameter *g*. The asymmetry parameter is well related to the radiative properties. Therefore the algorithm is again very efficient as reported in Figure 4. Over the large range of simulated values, from 0.367 to 0.805, "best" and "average" solutions are returning almost perfectly the input values. Small discrepancies occur only for different wind speed conditions and when particles are small, as noted in Tables 5a and 5b. Uncertainty in the surface conditions leads to choosing the closest model with slightly different radiative properties. Standard deviations are small, which confirms that the problem is very well conditioned for this parameter.

5.2.5. Median radius and standard deviation. From results reported in Table 5a it is obvious that the "best" model gives perfect results when the input parameters are included in the LUT. From results reported in Table 5b, which corresponds to input not included in the LUT, we also basically retrieve the right values except for the following cases: (1) model S_E instead of model S_B (cases 12 and 16), (2) model S_C instead of model S_A (cases 19, 21, and 24), and (3) model L_B instead of model L_A (case 21).

Referring to Tables 3a and 3b which give the properties of the models, it is clear that the alternative solutions correspond to aerosol models which have the closest radiative properties to those of the input models; that is, S_E and S_C have very similar effective radius to S_B and S_A, respectively, and L_B is similar to L_A. As shown in the work of *Tanré et al.*, [1996], we are in conditions where the driving parameter is the effective radius, and the exact values of the two parameters of the size distribution has no impact. There are conditions where single narrow size distributions could be retrieved [*Kaufman et al.*, 1990]. For instance, for smoke observed with scattering angles around 100° we should be able to distinguish between narrow and broad size distribution.

From Table 6a and 6b where "average" solutions are reported, the standard deviation computed for the median radius is usually small when a single mode is considered but becomes larger for double modes, mainly for the retrieval of the small mode r_m^s. As a general rule, the large mode is retrieved within the error bars, but larger discrepancies may be observed for the small mode.

5.3. Impact of Potential Sources of Error

In this section we discuss the impact of different types of errors (random, systematic, or spectrally dependent) that can be related to issues like the sensor calibration, the contamination by glint, or a wrong estimate of the water-leaving radiance.

Table 6b. Input and Retrieved Characteristics of Aerosol Models for "Average" Retrieval With Some Parameters Not Included in LUT

	Input Values				Retrieved Values			
Case	Median Radius r_m^s	s.d. σ^s	Median Radius r_m^l	s.d. σ^l	Median Radius r_m^s	s.d. σ^s	Median Radius r_m^l	s.d. σ^l
12	0.04	0.60	...	...	0.06 ± 0.02	0.50 ± 0.10	...	...
13	0.04	0.60	...	...	0.06 ± 0.02	0.50 ± 0.10	...	...
14	...	...	0.60	0.40	...	...	0.60 ± 0.00	0.40 ± 0.00
15	...	...	0.60	0.40	...	...	0.60 ± 0.00	0.40 ± 0.00
16	0.04	0.60	0.60	0.40	0.05 ± 0.03	0.51 ± 0.11	0.57 ± 0.08	0.43 ± 0.08
17	0.04	0.60	0.60	0.40	0.05 ± 0.03	0.51 ± 0.11	0.57 ± 0.08	0.43 ± 0.08
18	0.04	0.60	0.60	0.40	0.07 ± 0.02	0.53 ± 0.10	0.64 ± 0.22	0.60 ± 0.14
19	0.02	0.60	...	...	0.04 ± 0.00	0.40 ± 0.00		
20	...	...	0.40	0.60	...	...	0.50 ± 0.10	0.50 ± 0.10
21	0.02	0.60	0.40	0.60	0.06 ± 0.02	0.51 ± 0.10	0.67 ± 0.23	0.62 ± 0.14
22	0.02	0.60	...	...	0.03 ± 0.01	0.49 ± 0.10	...	...
23	...	...	0.60	0.80	...	...	0.70 ± 0.19	0.75 ± 0.09
24	0.02	0.60	0.60	0.80	0.06 ± 0.02	0.51 ± 0.10	0.78 ± 0.21	0.75 ± 0.09
25	0.02	0.60	0.60	0.80	0.03 ± 0.01	0.50 ± 0.11	0.70 ± 0.19	0.70 ± 0.11

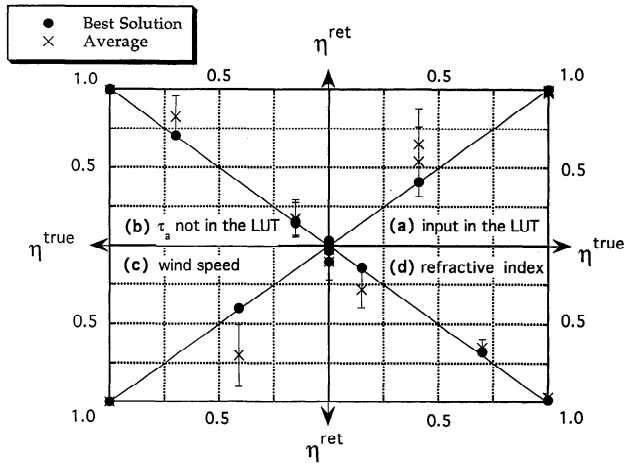

Figure 2. Same as in Figure 1 but for the ratio η.

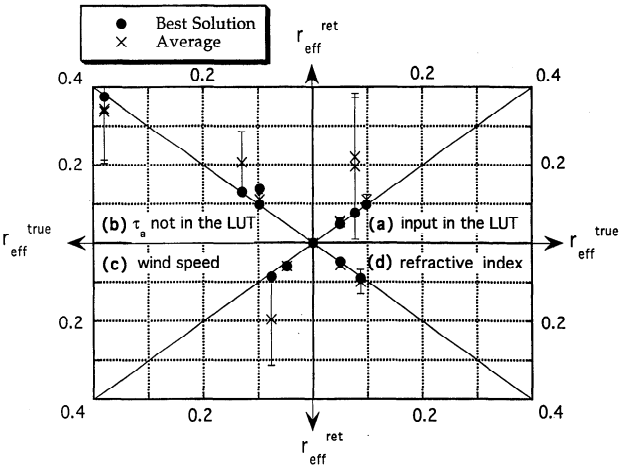

Figure 3b. Same as in Figure 3a but for effective radius smaller than 0.40 μm.

These effects are simulated by adding an error to the measurements L_j^m in channel j in the following way: (1) for calibration error, $L_j^m = >L_j^m(1. - \text{Rnd}_j)$, where Rnd_j is a randomly distributed number between ± 0.01; it represents a random spectral calibration error of 1%; (2) for glint error, $L_j^m = >L_j^m + 0.01$; this test considers that the glint may not be completely avoided or predicted, which adds a constant value to the reflectance in all channels; (3) for type 1 surface error, $L_j^m = >L_j^m + \text{Rnd}_j$, where Rnd_j is a randomly distributed number between ± 0.002; it represents, for instance, possible errors in the water-leaving radiance; (4) for type 2 surface error, $L_j^m = L_j^m + 0.005/\lambda_j$ with λ_j expressed in micrometers; the reflectance is increased by around 0.010 at 550 nm and 0.0025 at 2130 nm; it represents systematic errors in the spectral dependence of the reflectances, like uncertainties resulting from the foam spectral dependence.

In Figures 5–8, the quarters a, b, c, and d show the results for calibration errors, glint errors, and types 1 and 2 surface errors, respectively. Results are given for all cases (1–25), i.e., for input data sets which are included or not included in the LUT.

5.3.1. Optical thickness τ_a. For randomly distributed errors (quarters a and c in Figure 5) there is no systematic effect, and the impact is almost negligible in most cases. Surface errors due to the glint or due to type 2 surface errors lead to an overestimate of the optical thickness as reported in quarters b and d. The additional surface contribution is translated into a larger atmospheric contribution, which results in a larger optical thickness. This effect is more important for the small optical thickness values, i.e., $\tau = 0.20, 0.35$, or 0.50 than for the large values, i.e., $\tau = 0.85$ and 1.00.

It is clear that the ability to retrieve any information about the aerosols is greatly diminished when the aerosol optical thickness approaches very small values. In the algorithm, when the aerosol contribution is smaller than a third of the molecular contribution at 865 nm, the inversion is not performed. If aerosol contribution is comparable to the molecular contribution, only the aerosol optical thickness is derived and there is no derivation of the aerosol size distribution.

5.3.2. Ratio η. Figure 6 clearly shows that it will be difficult to retrieve this parameter accurately. The dispersion is quite large for both "best" and "average" solutions, thus the retrieved values will have to be considered as an estimate. Let us notice that the glint effect is the most destructive error; it may result in 100% error, and there is no systematic bias. Better values of the ratio η will be retrieved far from the specular reflection, a fact that will be considered in generating aerosol climatologies from the MODIS data.

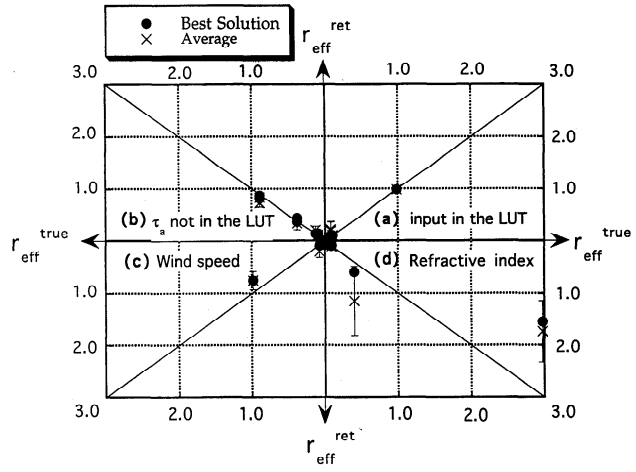

Figure 3a. Same as in Figure 1 but for the effective radius.

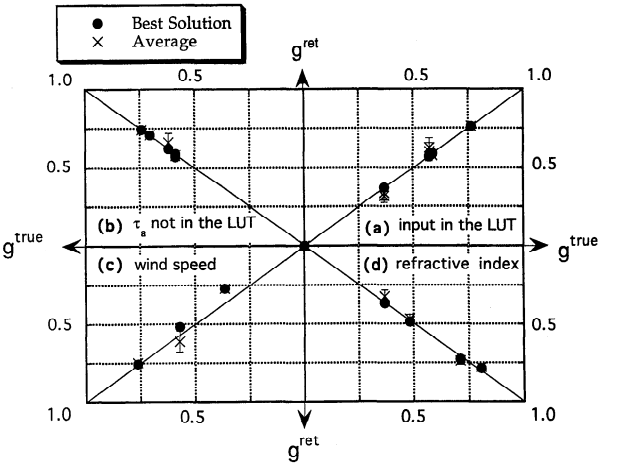

Figure 4. Same as in Figure 1 but for the asymmetry factor g.

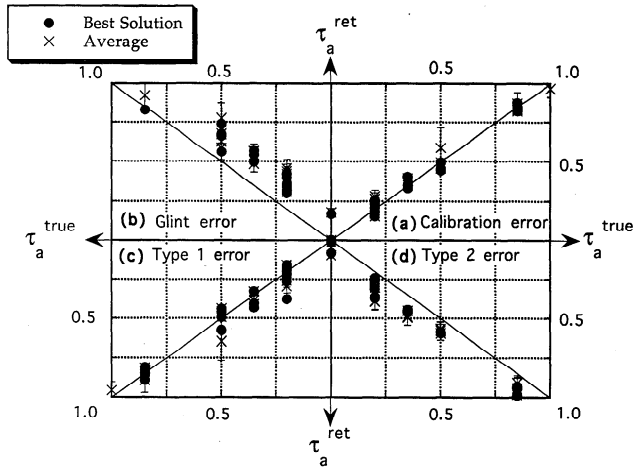

Figure 5. Scatter diagram of the optical thickness; the x axis corresponds to the input and the y axis to the retrieved values. Each quarter is devoted to a specific source of errors: Quarter a corresponds to calibration errors. Quarter b corresponds to glint error. Quarter c corresponds to type 1 surface error. Quarter d corresponds to type 2 surface error. The black dots correspond to the "best" model and the crosses to the "average" solution (see text). Error bars correspond to the standard deviation of the "average" solution.

5.3.3. Effective radius r_{eff}. For effective radii smaller than 0.2 μm (Figure 7b), only glint error leads to a significant impact for both "best" and "average" solutions. For other types of errors the best solution (black dots) is giving the right answer, while the average solution (crosses) shows a very large variability. For large effective radii (Figure 7a), all the different sources of errors result in an underestimate of the aerosol size. As mentioned in section 5.2.3, the sensitivity to large particles is weak, and there is a threshold value of the effective radius around 1.0 μm from which the retrieved value is questionable.

5.3.4. Asymmetry parameter g. The presence of errors does not affect the conclusions made in section 5.2.4. The retrieval of the asymmetry parameter is still very reliable (Figure 8). Again the glint error affects more intensively the results than the other sources of errors but in a nonsystematic way.

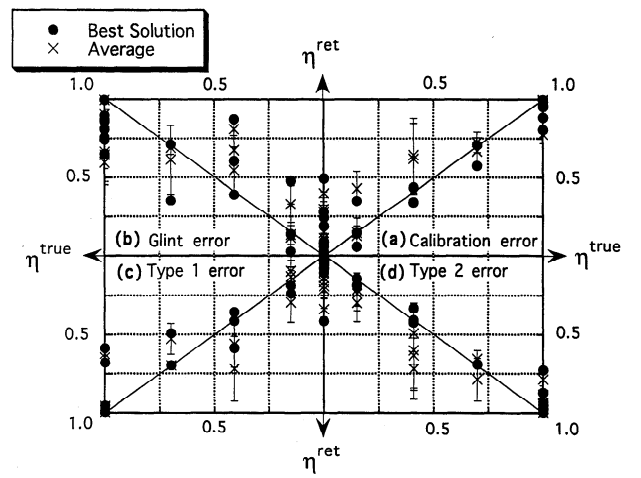

Figure 6. Same as in Figure 5 but for the ratio η.

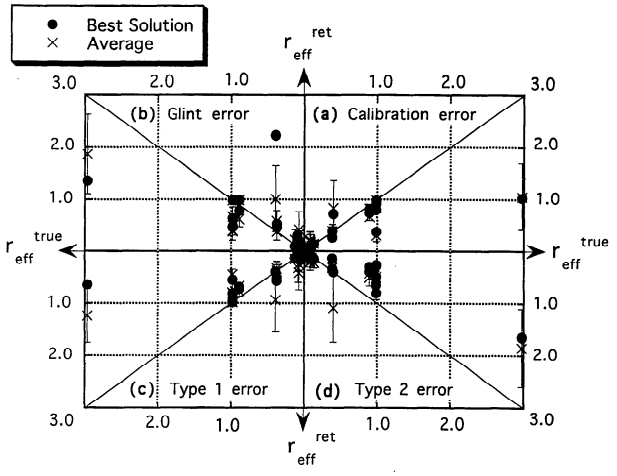

Figure 7a. Same as in Figure 5 but for the effective radius.

6. Application and Validation

The algorithm has been applied to thematic mapper data on Landsat 5 which has similar VIS, NIR, and SWIR spectral bands to MODIS (except the band at 1.240 μm). It has been also applied to the MODIS airborne simulator (MAS) data [*King et al.*, 1996]. Three types of aerosols have been considered, mineral dust coming from Africa, industrial/urban aerosol plumes, and smoke plumes resulting from logging waste fires.

6.1. Dust Over the Tropical Atlantic Ocean Near the Senegal Coast

Two field campaigns have been conducted in M'Bour, 80 km south of Dakar, Senegal in 1986 and 1987. Ground-based measurements, including spectral optical thickness, aureole, and downward sky radiances, have been performed [*Tanré et al.*, 1988a]. Four TM image data that correspond to the time of the ground-based measurements were acquired [*Tanré et al.*, 1988b], one in 1986 on April 30 and three in 1987 on April 1, 17, and May 3. Different dust loading conditions were observed with aerosol optical thickness at 550 nm varying between 0.55 and 2.40 (Table 7a). The larger values of the optical thickness were due to higher concentration of large dust par-

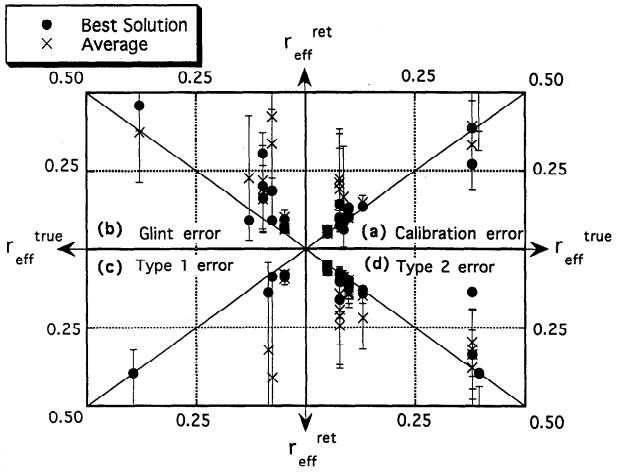

Figure 7b. Same as in Figure 7a but for effective radius smaller than 0.40 μm.

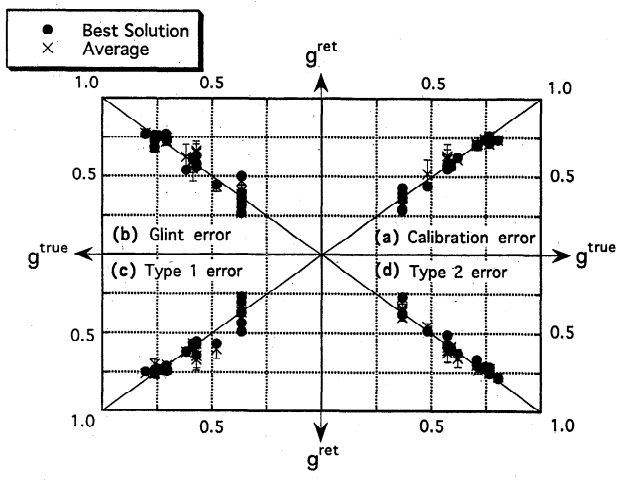

Figure 8. Same as in Figure 5 but for the asymmetry factor g.

ticles [*d'Almeida*, 1987; *Tanré et al.*, 1988a]. The TM reflectances computed over 10 boxes, with a size of 10 × 10 pixels in each, are reported in Table 7b as well as the standard deviation. Although they are not used in the inversion, values at 470 nm are also provided. As expected, the reflectances are increasing as a function of the optical thickness. Note the flatter spectral dependence observed on April 17, 1987, due to the presence of dust plume with the largest particles. The boxes have been chosen several kilometers away from the coast (Figure 9) to avoid adjacency effects as well as oceanic turbidity. The uniformity of the aerosol layer on April 30, 1986, is confirmed by the small standard deviation. Variability is larger for the other days, but the standard deviation remains less than 5% of the signal. It is still quite acceptable for deriving a mean value over the boxes. There may be cases where a mean value over a box has no significance, for example, when a dust front is within the box. Such cases are discriminated in the algorithm.

Results of the inversion are reported in Table 8a for the "best" model and in Table 8b for the "average" model. The "average" value has been computed according to its definition given in section 4.2, i.e., that the average is performed over the retrieved models as long as ε is smaller than 3%. When the minimum value of ε (reported in the Table 8a as ε_{min}) is already larger than 3%, the average is computed over the next five best solutions but stopping the averaging process as soon as ε is larger than 10%. The resulting maximum value of ε, noted as ε_{max}, is reported in Table 8b. Optical thickness values retrieved from the "best" model (Table 8a) are remarkably in

Table 7a. Aerosol Optical Thickness Measured at 550 nm in M'Bour During Field Experiments in 1986 and 1987

Day	Ground-Based Optical Thickness, 550 nm
April 30, 1986	0.55
April 1, 1987	1.47
April 17, 1987	2.40
May 3, 1987	0.84

a good agreement with the ground-based measurements when values of ε_{min} are small as for April 1, 1987. For April 30, 1986, and May 3, 1987, the results are also close to the ground measurements, but the fairly large value of ε_{min} seems to indicate that the present LUT does not include the most suitable aerosol models for these days. Results for April 17, 1987, are not significant since the existing LUT does not include optical thickness larger than 2.0; therefore the algorithm is forced to extrapolate linearly the optical thickness which results in an overestimated value. For the other aerosol parameters we do not have ground-based measurements for validating the results, but the general behavior is in a good agreement with what is expected: particles are bigger for larger optical thickness and biggest for April 17, 1987, with the dust plume. The ratio between small and large modes and the asymmetry factor have the right tendency as a function of the optical thickness. *Shettle* [1984], for instance, is suggesting values of 0.70 and 0.87 for asymmetry parameter for background desert and desert dust storm models. These values can be compared with 0.69 and 0.76 retrieved for the clearest and haziest days. Let us mention that the temporal evolution of the aerosol size retrieved from the TM images was confirmed by the aureole measurements that were performed during the experiment [*Tanré et al.*, 1988b]. Results for the "average" model (Table 8b) confirm the results of the sensitivity study; optical thickness and asymmetry parameters display small standard deviations when values of r_{eff} and η are more variable. As an example, for April 1, 1987, the effective radius and the ratio η are estimated within 43 and 40% when the optical thickness and the asymmetry parameter are estimated within 4 and 3%. This is confirmed by the results obtained on May 3, 1987, but it is less clear for April 30, 1986, where the accuracy is also good for the ratio η and the effective radius. Again optical thickness for April 17, 1987, is not significant since the retrieved value corresponds to the limits of the present LUT.

Table 7b. Mean Reflectances Expressed in Percent and Standard Deviations in Thematic Mapper (TM) Solar Spectral Bands Over Tropical Atlantic Ocean Close to Senegal Seashore

TM Band, nm	Mean Reflectance and s.d., April 30, 1986	Mean Reflectance and s.d., April 1, 1987	Mean Reflectance and s.d., April 17, 1987	Mean Reflectance and s.d., May 3, 1987
470	11.78 ± 0.11	16.26 ± 0.49	18.96 ± 0.08	13.84 ± 0.10
550	8.35 ± 0.16	13.52 ± 0.58	19.55 ± 0.22	10.34 ± 0.21
650	6.54 ± 0.10	12.48 ± 0.51	20.84 ± 0.24	8.87 ± 0.17
865	5.21 ± 0.09	11.24 ± 0.51	21.61 ± 0.32	8.03 ± 0.29
1600	2.69 ± 0.07	6.86 ± 0.32	16.67 ± 0.32	4.10 ± 0.14
2200	1.95 ± 0.04	5.54 ± 0.28	15.18 ± 0.30	3.20 ± 0.09

Average is performed over 10 oceanic targets whose size is 10 × 10 pixels (300 m × 300 m).

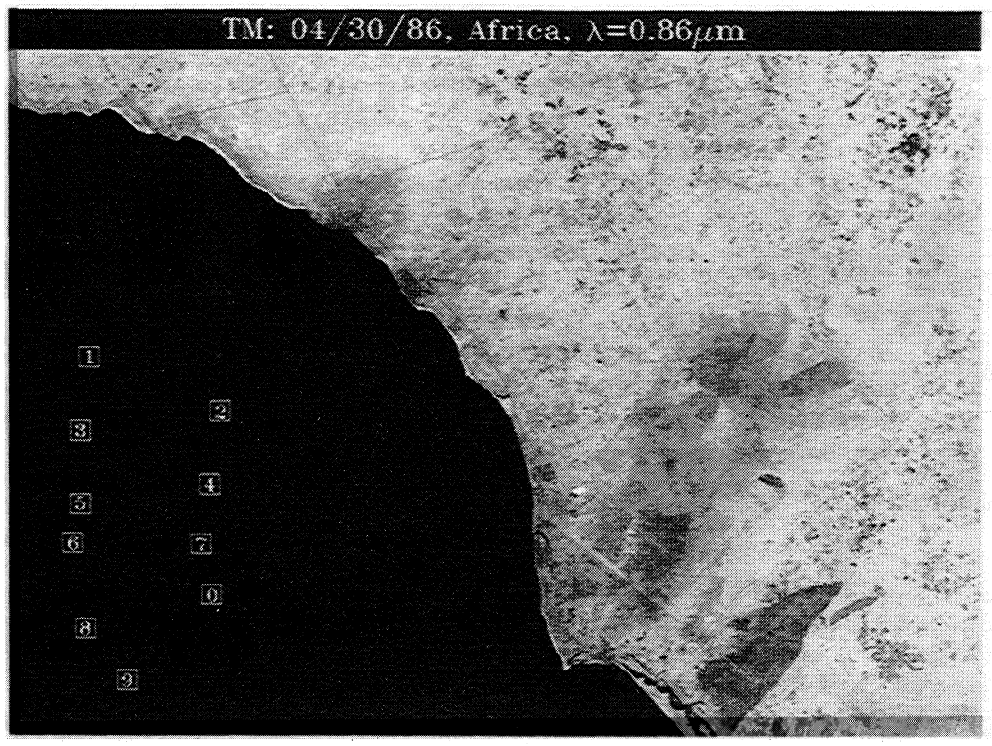

Figure 9. Thematic Mapper (TM) image on April 30, 1986 in band TM4 (865 nm) over the tropical Atlantic Ocean, near the Senegal coast, showing the locations of the 10 targets.

6.2. Sulfate Aerosols Over the Atlantic Ocean Near the U.S. East Coast

The Sulfate Cloud and Radiation experiment—Atlantic (SCAR A) was conducted July 1993 in the eastern United States Atlantic region. It was designed to measure the properties of urban and industrial pollution dominated by sulfate particles [*Remer et al.*, this issue]. The SCAR A experiment included a full integration of the operations of the Aerosol Robotic Network (AERONET), a field network of Sun-sky radiometers [*Holben et al.*, 1996], an instrumental C-131A aircraft with in situ and radiometric measurements [*Hegg et al.*, 1995] and the NASA ER-2 aircraft instrumented with the MODIS airborne simulator (MAS) and the airborne visible infrared imaging spectrometer (AVIRIS). Measurements were conducted during relatively clear and hazy conditions and in the presence and absence of clouds. NOAA/AVHRR and Landsat 5/TM images were acquired. Although the MAS data are available, they are not used hereinafter because of calibra-

Table 8a. Aerosol Parameters Retrieved From "Best" Aerosol Model for Four TM Images Acquired Over Tropical Atlantic Ocean

Day	τ^m, 550 nm	τ^r, 550 nm	r_{eff}	g	η	ε_{min}, %
April 30, 1986	0.55	0.66	0.29	0.73	0.62	6.1
May 3, 1987	0.84	1.08	0.39	0.73	0.42	7.3
April 1, 1987	1.47	1.51	0.51	0.74	0.25	1.3
April 17, 1987	2.40	3.36	0.98	0.76	0.00	4.2

Table 8b. Aerosol Parameters Retrieved From "Average" Aerosol Model for Four TM Images Acquired Over Tropical Atlantic Ocean

Day	τ^m, 550 nm	τ^r, 550 nm	r_{eff}	g	η	ε_{max}, %
April 30, 1986	0.55	0.61 ± 0.08 (13)	0.26 ± 0.04 (15)	0.69 ± 0.04 (6)	0.61 ± 0.08 (13)	8.8
May 3, 1987	0.84	1.02 ± 0.13 (13)	0.31 ± 0.10 (32)	0.70 ± 0.03 (4)	0.32 ± 0.15 (47)	9.9
April 1, 1987	1.47	1.43 ± 0.06 (4)	0.35 ± 0.15 (43)	0.71 ± 0.02 (3)	0.15 ± 0.06 (40)	3.0
April 17, 1987	2.40	3.36 ± 0.00 (N/A)	0.98 ± 0.00 (N/A)	0.76 ± 0.00 (N/A)	0.00 ± 0.00 (N/A)	4.2

Number in parentheses is the standard deviation divided by the mean (in percent).

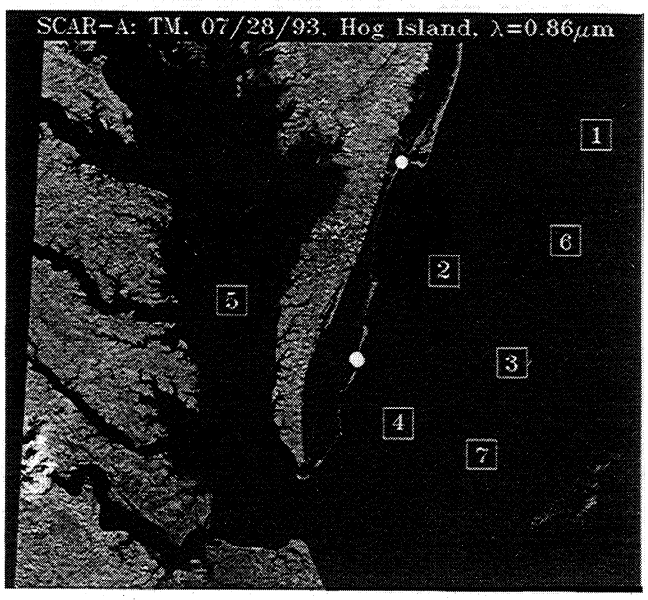

Figure 10. TM image on July 28, 1993 in band TM4 (865 nm) over the Atlantic Ocean, near the United States eastern seaboard, showing the locations of the seven selected zones. The two white dots correspond to the locations of the Sun photometers.

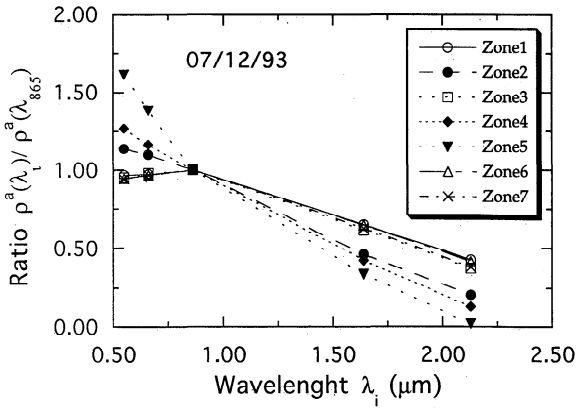

Figure 11a. TM reflectances normalized at 865 nm as a function of the wavelength for the seven zones on July 12, 1993.

tion problems. SCAR A was one of the first MAS campaigns, and the calibration was not fully reliable at that time.

The AERONET Sun photometers were settled mostly along the Atlantic coast, with an instrument at Wallops (N37°56′, W75°28′) and one in Hog Island (N37°25′, W75°42′). The TM images were acquired in the same area. Figure 10 shows the locations of the Sun photometers and the locations of seven oceanic zones selected for the analysis. The TM pixel size has been adjusted to the MODIS resolution, and the box size is 10 km × 10 km. Zones 1, 6, 3, and 7 are on a line parallel to the seashore, 50 km from the coast. Zones 2 and 4 are also on a line parallel to the coast but closer, around 15–20 km from the coast. Zone 5 is within the Chesapeake Bay. Mean TM reflectances and standard deviations computed over the seven boxes are reported in Table 9a for July 12, 1993, and in Table 9b for July 23, 1993. Spectral reflectances for zones 2, 4, and 5 clearly show a strange behavior for both days. After subtracting the molecular component in each band, we plotted the reflectances, normalized at 865 nm, as a function of the wavelength in Figure 11a for July 12, 1993, and in Figure 11b for July 28, 1993. If the larger values of the normalized reflectance obtained at 0.55 and 0.65 μm could be explained by a larger water turbidity expected near the coast, we have no explanation for the small values observed at 1.64 and 2.13 μm over zones 2, 4, and 5 for both days. The spatial variability of the aerosol layer is not the issue. From Table 9a, by reporting the reflectance values over the boxes 1, 6, 2, 3, 4, and 7, it is clear that the aerosol layer on July 12, 1993, displays at 550 nm a smooth decrease from the North to the South confirmed by the ground-based measurement. It is no longer true at 1.64 and 2.13 μm, where the reflectances over zones 2 and 4 are much smaller than over the other zones. Same conclusion can be

Table 9a. Mean Reflectances Expressed in Percent and Standard Deviations in Thematic Mapper Solar Spectral Bands During SCAR A Experiment on July 12, 1993

Band, nm	Zone 1	Zone 2	Zone 3	Zone 4	Zone 5	Zone 6	Zone 7
550	7.87 ± 0.13	7.16 ± 0.13	6.99 ± 0.13	7.01 ± 0.16	7.74 ± 0.17	7.43 ± 0.14	6.64 ± 0.14
650	6.29 ± 0.12	5.43 ± 0.12	5.50 ± 0.07	5.10 ± 0.13	5.51 ± 0.08	5.91 ± 0.13	5.13 ± 0.14
865	5.31 ± 0.19	4.01 ± 0.19	4.47 ± 0.10	3.55 ± 0.19	3.39 ± 0.11	4.96 ± 0.17	4.14 ± 0.13
1600	3.01 ± 0.11	1.52 ± 0.13	2.33 ± 0.08	1.21 ± 0.18	0.91 ± 0.08	2.76 ± 0.07	2.16 ± 0.07
2200	1.97 ± 0.11	0.68 ± 0.15	1.41 ± 0.15	0.37 ± 0.19	0.06 ± 0.06	1.78 ± 0.16	1.32 ± 0.07

Average is performed over boxes whose size is 10 km × 10 km.

Table 9b. Mean Reflectances Expressed in Percent and Standard Deviations in Thematic Mapper Solar Spectral Bands During SCAR A Experiment on July 28, 1993

Band, nm	Zone 1	Zone 2	Zone 3	Zone 4	Zone 5	Zone 6	Zone 7
550	5.66 ± 0.06	4.76 ± 0.11	5.62 ± 0.17	4.80 ± 0.05	5.45 ± 0.13	5.63 ± 0.11	5.72 ± 0.18
650	4.26 ± 0.10	2.94 ± 0.22	4.02 ± 0.14	2.88 ± 0.14	3.45 ± 0.05	4.16 ± 0.12	4.01 ± 0.16
865	3.31 ± 0.16	1.64 ± 0.26	2.94 ± 0.18	1.59 ± 0.19	1.59 ± 0.09	3.14 ± 0.17	2.80 ± 0.20
1600	1.89 ± 0.11	0.20 ± 0.22	1.34 ± 0.13	0.08 ± 0.12	0.12 ± 0.10	1.66 ± 0.11	1.06 ± 0.11
2200	1.25 ± 0.13	0.001[a]	0.71 ± 0.13	0.001[a]	0.001[a]	1.00 ± 0.10	0.39 ± 0.12

Average is performed over boxes whose size is 10 km × 10 km.
[a]Because of calibration the reflectances over these targets were slightly negative and were put equal to 0.001.

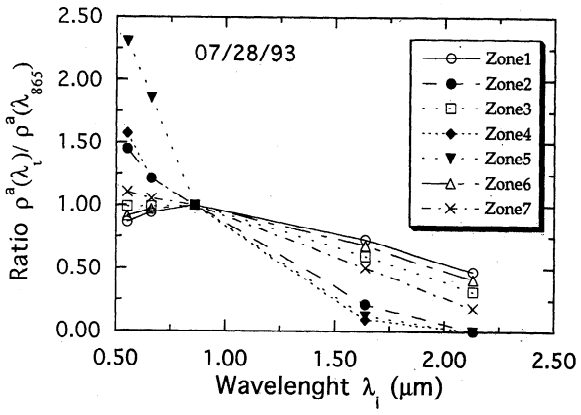

Figure 11b. Same as in Figure 11a but for July 28, 1993.

made on July 28, 1993. It could be due to instrumental problems, because of adjacent bright coast the instrument may have difficulty recovering from the large values over the land, resulting in an undershoot. Calibration is definitively an issue since we get slightly negative values on July 28, 1993, at 2.13 μm, but it cannot be the only explanation.

The retrieved aerosol parameters are reported in Table 10a for the "best" solution over the seven zones and the "average" performed over the five better solutions in Table 10b for zones 1, 3, 6, and 7 only. Table 10a reflects also the problem regarding zones 2, 4, and 5. We even cannot invert data on July 28, 1989, for these zones and on July 12, 1993, the very large values of ε_{min} proves that the results are not significant. Nevertheless, if we limit our analysis to zones 1, 6, 3, and 7, ground-based and retrieved optical thicknesses compare very well, even better for the "average" solution. The effective radii of both modes are quite stable for the four zones, 0.11–0.18 and 0.90–2.00 for the small and large modes, respectively (Table 10b). For comparison, measurements by the AERONET instrumentation reported effective radius of the accumulation mode in the range 0.16–0.18 on July 12 (0.11–0.16 in the present analysis), and 0.12–0.13 on July 28 (0.11–0.18 in the present analysis). The urban/industrial aerosol dynamic model [*Remer et al.*, this issue] identifies accumulation mode particles between 0.09 μm for very clear conditions and 0.19 μm in hazy conditions, as well as a maritime coarse particle mode at 1.2 μm.

On July 12, 1993, the latitudinal gradient of η between the southern and the northern zones is correlated to an increase in the optical thickness τ, $\eta = 0.73$ for $\tau = 0.48$ and $\eta = 0.47$ for $\tau = 0.62$ for the "best" solution; $\eta = 0.67$ for $\tau = 0.46$, and $\eta = 0.29$ for $\tau = 0.53$ for the "average" solution. Although these results are in agreement with *Remer et al.* [this issue], the present accuracy of our retrieval, as noted by the high values of ε_{min}, is not sufficient for making a definitive statement.

6.3. Smoke Over Pacific Ocean Near the U.S. West Coast

The Smoke Cloud and Radiation experiment—California (SCAR C) was conducted in September 1994 in the Pacific Northwest. It was designed to measure the entire process of biomass burning, including ground-based estimates of fuel consumption, airborne sampling of the smoke aerosol and trace gases, and airborne and spaceborne remote sensing of fires and smoke [*Kaufman et al.*, 1996]. Remote sensing images of fires and smoke were taken by MAS and AVIRIS flown on the ER-2 aircraft. We analyze the MAS data for the Quinault prescribed fire in Washington state using the observations performed from the ER-2 at 2030:54 GMT. The fire was lit very close to the seashore with wind transporting the smoke over the ocean. The fuel of this prescribed fire consisted of old-growth large western red cedar debris left over logging [*Hobbs et al.*, 1996]. Results are reported in Table 11 as a function of the distance from the fire. Note that for the prevailing wind of 7 ms^{-1}, smoke measured 25 km offshore represent smoke that is 1 hour old and that was emitted from the fire 1 hour earlier than the smoke observed close to the fire. The smoke plume shown in Figure 12 is narrow and nonuniform. Therefore application of the present algorithm may be limited by the assumption of a plane parallel atmosphere used in the generation of the lookup tables. Limitations in the calibration accuracy prohibited us to use the 1.64 and 2.13 μm channels. In these channels the smoke is very transparent with a very weak backscattered signal [*Kaufman*, 1993]. Therefore small calibration errors generated even negative values of the upward radiance in these channels.

The results show a very stable small particle mode with $r_{eff} = 0.06$ μm and a coarse particle mode with $r_{eff} = 2.5$ μm that disappeared 16 km (or 40 min) from the shore. Measurements of the particle size distributions from collections on nucleopore filters shows that the accumulation mode particle size distri-

Table 10a. Aerosol Parameters Retrieved From "Best" Aerosol Model for Two TM Images Acquired During SCAR A Experiment

Day	τ^m, 550 nm (Wallops)	τ^m, 550 nm (Hog Island)	τ^r, 550 nm	r_{eff}	g	η	ε_{min}, %
July 12, 1993	0.60 ± 0.04	0.57 ± 0.04	0.62 (zone 1)	0.36	0.73	0.47	8.9
			0.57 (zone 6)	0.34	0.73	0.50	10.0
			0.55 (zone 3)	0.26	0.73	0.71	12.8
			0.48 (zone 7)	0.26	0.72	0.73	12.9
			0.42 (zone 2)	0.12	0.57	1.00	22.0
			0.33 (zone 4)	0.12	0.57	1.00	31.6
			0.27 (zone 5)	0.06	0.27	1.00	51.9
July 28, 1993	0.20 ± 0.02	0.21 ± 0.01	0.26 (zone 1)	0.35	0.73	0.28	10.5
			0.30 (zone 6)	0.21	0.72	0.89	13.8
			0.21 (zone 3)	0.12	0.57	1.00	18.3
			0.18 (zone 7)	0.12	0.57	1.00	29.0
			N/A (zone 2)	...	...	...	...
			N/A (zone 4)	...	...	...	...
			N/A (zone 5)	...	...	...	...

Table 10b. Aerosol Parameters Retrieved From the Five "Best" Aerosol Models for Two TM Images Acquired During SCAR A Experiment

	τ^r, 550 nm	r^s_{eff}	r^l_{eff}	r_{eff}	η	$\varepsilon_{\max}$, %
July 12, 1993						
zone 1	0.53 ± 0.05	0.11 ± 0.06	0.90 ± 0.00	0.26 ± 0.08	0.24 ± 0.15	10.0
zone 6	0.52 ± 0.08	0.13 ± 0.05	0.92 ± 0.05	0.28 ± 0.08	0.36 ± 0.19	12.0
zone 3	0.52 ± 0.10	0.16 ± 0.05	1.04 ± 0.26	0.23 ± 0.03	0.66 ± 0.21	15.0
zone 7	0.46 ± 0.09	0.16 ± 0.05	1.04 ± 0.26	0.23 ± 0.03	0.67 ± 0.22	15.0
July 28, 1993						
zone 1	0.22 ± 0.02	0.11 ± 0.06	0.90 ± 0.00	0.32 ± 0.05	0.21 ± 0.18	11.0
zone 6	0.30 ± 0.05	0.18 ± 0.04	1.46 ± 0.09	0.20 ± 0.01	0.89 ± 0.17	14.0
zone 3	0.21 ± 0.00	0.12 ± 0.06	2.28 ± 1.74	0.12 ± 0.00	1.00 ± 0.00	18.3
zone 7	0.18 ± 0.00	0.12 ± 0.00	2.28 ± 1.74	0.12 ± 0.00	1.00 ± 0.00	29.0

bution varied from a radius of 0.06 μm for flaming conditions close to the fire to 0.14 μm for a mixed 2 hours old smoke [*Martins et al.*, 1996]. Large coarse particles were also observed in flaming conditions close to the fire. *Hobbs et al.* [1996] analyzed the in situ measurements of the size distribution of aerosol particles in these prescribed fires. From these measurements we can deduce that the particle size decreased from r_{eff} = 0.12 μm in the flaming stage to 0.10 μm in the smoldering stage. He also found the particle size to increase from r_{eff} = 0.11 μm for fresh flaming aerosol to 0.17 two hours later. These particle sizes are somewhat larger than the size derived from the remote sensing data, but direct validation of the particle size in the whole vertical column is not available. The finite horizontal dimensions of the smoke plume are expected to affect the longer wavelengths more than the shorter wavelengths due to the spectral variability of the smoke opacity. This may result in artificially smaller particles.

In summary, the remote sensing data depicted correctly the reduction in the particle size from the urban/industrial haze aerosol to the smoke aerosol. This reduction is consistent also with the dynamic aerosol models for both conditions with r_{eff} = 0.19 μm for the urban/industrial haze aerosol in the mid-Atlantic region of the United States and 0.11 μm for mixed smoke aerosol in South America [*Remer et al.*, 1996].

7. Discussion

The present comparison of the field experiment data with the retrieved aerosol parameters is very encouraging. See, for instance, Figure 13, which summarizes the optical thickness results for both the African and the SCAR A data. Nevertheless, testing the algorithm with actual data has disclosed several problems in the present scheme: (1) the maximum value of the optical thickness (τ_a = 2.0) has to be increased to deal with large mineral dust plumes as well as with smoke plumes; (2) the uniformity of the aerosol layer within the box, aerosol content, or aerosol type can be a problem at a scale of 50 × 50 km^2; (3) additional aerosol models need to be included in the LUT, refractive index, or size distribution to better fit the spectral radiances. The choice of the width of the size distribution σ is not crucial so long as the right values of the effective radius are included [*Kaufman et al.*, 1990; *Tanré et al.*, 1996]. Regarding the surface properties, the water-leaving radiance at 555 nm is well determined for pigment concentrations up to 0.5 mg/m^3 but is affected by fluctuations for larger concentrations [*Gordon*, 1996]. This channel may not be used in the algorithm over waters known to be very productive so long as an estimate of the concentration is not available. It would affect the retrieval of the small mode. There are also improvements that can be easily implemented; we can add to the LUT an intermediate value of η (η = 0.5) to reduce the possible errors introduced in the retrieval by the use of (6).

Additional issues, although not discussed in this paper, have also to be addressed in the future. When volcanic eruptions occur, like the most recent Pinatubo eruption in June 1991, they generate a large amount of aerosols within the stratosphere. Already a few weeks after an eruption, the stratospheric component can be larger than the tropospheric signal that we are analyzing, and a correction has to be made. It could be done using the data provided by the sensors using the solar occultation approach [*Kent et al.*, 1988; *McCormick and Veiga*, 1992] or given by the 1.37 μm channel on MODIS for cirrus and stratospheric aerosol detection [*Gao and Kaufman*, 1995]. The number of cloud-free pixels within the box is also an important question, as is the maximum percentage of cloud cover we accept for making the inversion. Depending on the point spread function (PSF) of the instrument, the minimum

Table 11. Aerosol Parameters Retrieved From Five "Best" Aerosol Models for MAS Data Acquired During SCAR C Experiment

Distance, km	r^s_{eff}	r^l_{eff}	r_{eff}	g	τ	η	ε, %
5	0.06 ± 0.00	2.48 ± 1.68	0.082 ± 0.028	0.34	2.59 ± 0.14	0.86 ± 0.02	1.0
8	0.06 ± 0.00	2.48 ± 1.68	0.067 ± 0.011	0.30	2.12 ± 0.04	0.95 ± 0.01	1.2
16	0.06 ± 0.00	2.48 ± 1.68	0.060 ± 0.000	0.27	1.55 ± 0.00	1.00 ± 0.00	3.2
20	0.06 ± 0.00	2.48 ± 1.68	0.060 ± 0.000	0.27	1.07 ± 0.00	1.00 ± 0.00	5.4
28	0.06 ± 0.00	2.48 ± 1.68	0.060 ± 0.000	0.27	1.10 ± 0.00	1.00 ± 0.00	7.0
36	0.06 ± 0.00	2.48 ± 1.68	0.060 ± 0.000	0.27	1.05 ± 0.00	1.00 ± 0.00	9.8
44	0.06 ± 0.00	2.48 ± 1.68	0.060 ± 0.000	0.27	1.34 ± 0.00	1.00 ± 0.00	3.5

The ε is computed over three spectral bands, i.e., 550, 659, and 865 nm.

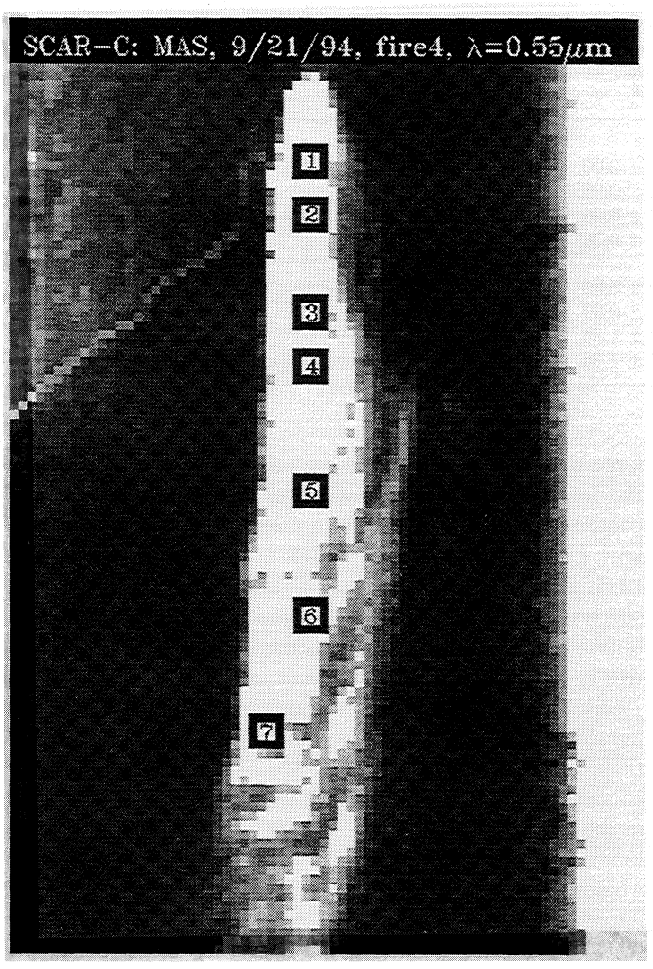

Figure 12. MODIS airborne simulator image on September 21, 1994, at 550 nm over the Pacific Ocean, near the United States western seaboard, showing the locations of the seven zones within the smoke plume.

distance between the cloud-free pixels and the edge of a cloud is also an issue. A compromise has to be found for performing good retrieval without applying too restrictive conditions.

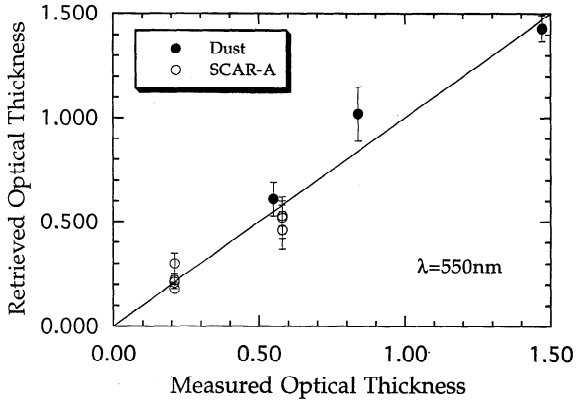

Figure 13. Comparison between the aerosol optical thickness measured at the ground level and the aerosol optical thickness retrieved from TM data for the African and SCAR A experiments.

8. Conclusion

The present study has confirmed the potential of MODIS for retrieving the aerosol parameters like the optical thickness and the asymmetry parameter, the domination of the accumulation or coarse mode, and to a lesser extent the ratio between the modes and the size of the main mode. When the spectral measurements are similar to a model included in the LUT, then the optical thickness is very well retrieved. In this regard, $\varepsilon_{\min}$ values are a good indicator of the quality of the retrieval. The size of particles is also fairly well monitored, as shown by the results obtained for the different aerosol types. A first rough estimate of the general accuracy is $\Delta\tau = \pm 0.05 \pm 0.5\tau$ (at 550 nm), $\Delta r_m = \pm 30\%$, $\Delta\eta = \pm 0.25$, and $\Delta g = \pm 0.03$.

The quality of the inversion strongly depends on the quality of inputs used to build the LUT. Surface contribution is a major issue; the spectral reflectance of the foam has to be accurately determined; wind speed estimated from general circulation models and water-leaving radiance should be preferably estimated from MODIS itself or at least from standard ocean color maps. Glint mask has also to be efficient because glint uncertainty results in very large errors. The AERONET Sun photometer network has to be maintained and extended for a better characterization of the aerosol particles.

The philosophy used to build our algorithm has been shown quite adequately. After its validation the aerosol information derived from MODIS should be very well adapted for studying aerosol climatology, i.e., to monitor the sources, the transport and the sinks of specific aerosol types, the interaction of aerosol with water vapor and clouds (both monitored by MODIS), and finally their radiative forcing.

Appendix

Optical Properties

1. The asymmetry factor is defined by [*Chandrasekhar*, 1960]

$$g_\lambda = \frac{1}{2}\int_{-1}^{+1} \mu P_\lambda(\mu)\, d\mu \tag{A1}$$

where $P_\lambda(\mu)$ is the aerosol phase function and μ is the cosine of the scattering angle. The asymmetry factor of the total size distribution is obtained from

$$g_\lambda = \frac{\omega_{0\lambda}^s \tau_\lambda^s g_\lambda^s + \omega_{0\lambda}^l \tau_\lambda^l g_\lambda^l}{\omega_{0\lambda}^s \tau_\lambda^s + \omega_{0\lambda}^l \tau_\lambda^l} \tag{A2}$$

where g_λ^s and g_λ^l are the asymmetry factors of each mode; $\omega_{0\lambda}^s$ and $\omega_{0\lambda}^l$ are the single-scattering albedos; τ_λ^s and τ_λ^l are the optical thicknesses.

2. The backscattering ratio β_λ is defined by [*Wiscombe and Grams*, 1976]

$$\beta_\lambda = \frac{1}{2\pi}\int_{-1}^{+1} \mu^{-1} P_\lambda(\mu)\, d\mu \tag{A3}$$

The backscattering ratio of the total size distribution is then obtained from

$$\beta_\lambda = \frac{\omega_{0\lambda}^s \tau_\lambda^s \beta_\lambda^s + \omega_{0\lambda}^l \tau_\lambda^l \beta_\lambda^l}{\omega_{0\lambda}^s \tau_\lambda^s + \omega_{0\lambda}^l \tau_\lambda^l} \tag{A4}$$

where β_λ^s and β_λ^l are the backscattering ratio of each mode.

Physical Properties

1. The moments M_k of the order of k are defined by

$$M_k = \int_0^\infty r^k n(r)\, dr \tag{A5}$$

which for a lognormal distribution gives

$$M_k = = r^k \exp\{\tfrac{1}{2}k^2 \ln^2(\sigma)\} \tag{A6}$$

It allows us to compute the effective radius r_{eff} and the effective variance of the size distribution which are respectively given by

$$r_{\text{eff}} = \frac{N^s M_3^s + N^l M_3^l}{N^s M_2^s + N^l M_2^l} \tag{A7a}$$

$$\sigma_{\text{eff}} = \frac{N^s M_4^s + N^l M_4^l}{N^s M_2^s + N^l M_2^l} \tag{A7b}$$

2. The number of cloud condensation nuclei of the small mode, N_{CCN}, is defined by

$$N_{\text{CCN}} = N^s \int_{r_0}^\infty n^s(r)\, dr = N^s 0.5(1 - \text{erf}(A)) \tag{A8}$$

where $r_0 = 0.03$ μm and $A = (1/(2)^{1/2})(\ln(r_0/r_m^s)/\ln(\sigma^s))$.

Acknowledgments. The satellite data have been processed by Li Rong-Rong at the GSFC/NASA; her help is gratefully acknowledged. The authors would like to thank L. A. Remer and B. N. Holben at the GSFC/NASA for giving them access to the SCAR experiment data sets. They also wish to acknowledge H. R. Gordon for valuable discussions apart from the MODIS meetings. This study has been funded by NASA (National Aeronautics and Space Administration) under the EOS program and by CNES (Centre National d'Etudes Spatiales), the French Space Agency. One of us (DT) would like to thank USRA for its support and the Climate and Radiation Branch in GSFC/NASA for its kind hospitality. Comments and suggestions from the reviewers are greatly appreciated.

References

Ahmad, Z., and R. S. Fraser, An iterative radiative transfer code for ocean-atmosphere system, *J. Atmos. Sci.*, *39*, 656–665, 1982.

Carlson, T. N., Atmospheric turbidity in Saharan dust outbreaks as determined by analyses of satellite brightness data, *Mon. Weather Rev.*, *107*, 322–335, 1979.

Chandrasekhar, S., *Radiative Transfer*, 393 pp., Dover, Mineola, N. Y., 1960.

Cox, C., and W. Munk, Statistics of the sea surface derived from sun glitter, *J. Mar. Res.*, *13*, 198–208, 1954.

d'Almeida, G. A., On the variability of desert aerosol radiative characteristics, *J. Geophys. Res.*, *93*, 3017–3026, 1987.

Deschamps, P. Y., F. M. Bréon, M. Leroy, A. Podaire, A. Bricaud, J. C. Buriez, and G. Sèze, The POLDER mission: Instrument Characteristics and Scientific Objectives, *IEEE Trans. Geosci. Remote Sens.*, *32*, 598–615, 1994.

Deuzé, J. L., F. M. Bréon, P. Y. Deschamps, C. Devaux, M. Herman, A. Podaire, and J. L. Roujean, Analysis of the POLDER (Polarization and Directionality of Earth's Reflectances) airborne instrument, *Remote Sens. Environ.*, *45*, 137–154, 1993.

Diner, D. J., et al., MISR: A Multiangle Imaging SpectroRadiometer for geophysical and climatological research from EOS, *IEEE Trans. Geosci. Remote Sens.*, *27*, 200–214, 1989.

Dulac, F., D. Tanré, G. Bergametti, P. Buat-Menard, M. Desbois, and D. Sutton, Assessment of the African airborne dust mass over the western Mediterranean sea using Meteosat data, *J. Geophys. Res.*, *97*, 2489–2506, 1992.

Durkee, P. A., Aerosol characteristics with dual wavelength radiance measurements, in *Remote Sensing and Applications*, Am. Meteorol. Soc., Boston, Mass., 1985.

Fraser, R. S., Satellite measurement of mass of Saharan dust in the atmosphere, *Appl. Opt.*, *15*, 2471–2479, 1976.

Frouin, R., M. Schwindling, and P. Y. Deschamps, Spectral reflectance of sca foam in the visible and near-infrared: In situ measurements and Remote Sensing implications, *J. Geophys. Res.*, *101*, 14,361–14,371, 1996.

Gao, B. C., and Y. J. Kaufman, Selection of the 1.375 μm MODIS channel for remote sensing of cirrus clouds and stratospheric aerosols from space, *J. Atmos. Sci.*, *52*, 4231–4237, 1995.

Gordon, H. R., Diffuse reflectance of the ocean: The theory of its augmentation by chlorophyll *a* fluorescence at 685 nm, *Appl. Opt.*, *18*, 1161–1166, 1979.

Gordon, H. R., Atmospheric correction of ocean color imagery in the EOS era, *J. Geophys. Res.*, this issue.

Griggs, M., Satellite observations of atmospheric aerosols during the EOMET cruise, *J. Atmos. Sci.*, *36*, 695–698, 1979.

Hansen, J. E., and Hovenier, J. W., Interpretation of the polarization of Venus, *J. Atmos. Sci.*, *31*, 1137–1160, 1974.

Hegg, D. A., P. V. Hobbs, R. J. Ferek, and A. P. Waggoner, Measurements of some aerosol properties relevant to radiative forcing on the east coast of the United States, *J. Appl. Meteorol.*, *34*, 2306–2315, 1995.

Hidy, G. M., *Aerosols: An Industrial and Environment Science*, 774 pp., Academic, San Diego, Calif., 1984.

Hobbs, P. V., J. S. Reid, J. A. Herring, J. D. Nance, R. E. Weiss, J. L. Ross, D. A. Hegg, R. D. Ottmar, and C. Louisse, Particle and trace gas measurements in the smoke from prescribed burns of forest products in the Pacific Northwest, *Global Biomass Burning*, J. Levin (Ed.), pp 697–715, MIT Press, Cambridge, Mass., 1996.

Holben, B. N., Y. J. Kaufman, A. Setzer, D. Tanré, and D. Ward, Optical properties of aerosol emissions from biomass burning in the tropics—BASE-A, in *Global Biomass Burning: Atmospheric, Climate and Biospheric Implications*, edited by J. Levine, pp. 403–411, MIT Press, Cambridge, Mass., 1991.

Holben, B. N., et al., Multi-band automatic Sun and sky scanning radiometer system for measurements of aerosols, *Remote Sens. Environ.*, in press, 1996.

Hoppel, W. A., J. W. Fitzgerald, G. M. Frick, R. E. Larson, and E. J. Mack, Aerosol size distribution and optical properties found in the marine boundary layer over the Atlantic Ocean, *J. Geophys. Res.*, *95*, 3659–3686, 1990.

Jankowiak, I., and D. Tanré, Climatology of Saharan dust events observed from Meteosat imagery over Atlantic Ocean, Method and preliminary results, *J. Clim.*, *5*, 646–656, 1992.

Junge, C. E., *Air Chemistry and Radioactivity*, 374 pp., Academic, San Diego, Calif., 1963.

Kahn, R., R. West, D. McDonald, B. Rheingans, and M. I. Mishchenko, Sensitivity of multiangle remote sensing observations to aerosol sphericity, *J. Geophys. Res.*, this issue.

Kaufman, Y. J., Aerosol optical thickness and atmospheric path radiance, *J. Geophys. Res.*, *98*, 2677–2692, 1993.

Kaufman, Y. J., and B. N. Holben, Hemispherical backscattering by biomass burning and sulfate particles derived from sky measurements, *J. Geophys. Res.*, *101*, 19,433–19,445, 1996.

Kaufman, Y. J., R. S. Fraser, and R. A. Ferrare, Satellite measurements of large-scale air pollution methods, *J. Geophys. Res.*, *95*, 9895–9909, 1990.

Kaufman, Y. J., A. Gitelson, A. Karnieli, E. Ganor, R. S. Fraser, T. Nakajima, S. Mattoo, and B. N. Holben, Size distribution and phase function of aerosol particles retrieved from sky brightness measurements, *J. Geophys. Res.*, *99*, 10,341–10,356, 1994.

Kaufman, Y. J., L. A. Remer, R. D. Ottmar, D. E. Ward, R.-R. Li, R. Kleidman, R. S. Fraser, L. Flynn, D. McDougal, and G. Shelton, Relationship between remotely sensed fire intensity and rate of emission of smoke: SCAR-C experiment, in *Global Biomass Burning*, edited by J. Levin, pp. 685–696, MIT Press, Cambridge, Mass., 1996.

Kaufman, Y. J., D. Tanré, H. R. Gordon, T. Nakajima, J. Lenoble, R. Frouin, H. Grassl, B. M. Herman, M. D. King, and P. M. Teillet, Passive remote sensing of tropospheric aerosol and atmospheric correction for the aerosol effect, *J. Geophys. Res.*, this issue.

Kent, G. S., U. O. Farrukn, P. H. Wang, and A. Deepak, SAGE I and

SAM II measurements of 1.0 μm aerosol extinction in the free troposphere, *J. Appl. Meteorol.*, *27*, 269–278, 1988.

King, M. D., D. M. Byrne, B. M. Herman, and J. A. Reagan, Aerosol size distribution obtained by inversion of optical depth measurements, *J. Atmos. Sci.*, *35*, 2153–2167, 1978.

King, M. D., Y. Kaufman, P. Menzel, and D. Tanré, Remote sensing of cloud, aerosol and water vapor properties from the moderate resolution imaging spectrometer (MODIS), *IEEE Trans. Geosci. Remote Sens.*, *30*, 2–27, 1992.

King, M. D., et al., Airborne scanning spectrometer for remote sensing of cloud, aerosol, water vapor and surface properties, *J. Atmos. Oceanic Technol.*, *13*, 777–794, 1996.

Koepke, P., Effective reflectance of oceanic whitecaps, *Appl. Opt.*, *23*, 1816–1823, 1984.

Koepke, P., and M. Hess, Scattering functions of tropospheric aerosols: The effects of nonspherical particles, *Appl. Opt.*, *27*, 2422–2430, 1988.

Koepke, P., and H. Quenzel, Turbidity of the atmosphere determined from satellite calculation of optimum viewing geometry, *J. Geophys. Res.*, *84*, 7847–7855, 1979.

Martins, J. V., P. Artaxo, C. Liousse, H. Cachier, Y. Kaufman, and A. P. Fattori, Size distribution, elemental composition, carbon measurements and calculated optical properties of biomass burning aerosol particles during the SCAR-C experiment, in *Global Biomass Burning*, edited by J. Levin, pp. 716–732, MIT Press, Cambridge, Mass., 1996.

Martonchik, J. V., and D. J. Diner, Retrieval of aerosol optical properties from multi-angle satellite imagery, *IEEE Trans. Geosci. Remote Sens.*, *30*, 223–230, 1992.

McCormick, M. P., and R. E. Veiga, SAGE II measurements of early Pinatubo aerosols, *Geophys. Res. Lett.*, *19*, 155–158, 1992.

Mekler, Y., H. Quenzel, G. Ohring, and I. Marcus, Relative atmospheric aerosol content from ERTS observations, *J. Geophys. Res.*, *82*, 967–972, 1977.

Mézáros, E., Atmospheric Chemistry—Fundamental aspect, in *Studies in Environmental Science*, vol. 11, 201 pp., Elsevier Sci., New York, 1981.

Mishchenko, M. I., and L. D. Travis, Light scattering by polydispersions of randomly oriented spheroids with sizes comparable to wavelengths of observation, *Appl. Opt.*, *33*, 7206–7225, 1994.

Mishchenko, M. I., A. A. Lacis, B. E. Carlson, and L. D. Travis, Nonsphericity of dust-like tropospheric aerosols: Implications for aerosol remote sensing and climate modeling, *Geophys. Res. Lett.*, *22*, 1077–1080, 1995.

Morel, A., and L. Prieur, Analysis of variations in ocean color, *Limnol. Oceanogr.*, *22*, 709–722, 1977.

Nakajima, T., M. Tanaka, and T. Yamauchi, Retrieval of the optical properties of aerosols from aureole and extinction data, *Appl. Opt.*, *22*, 2951–2959, 1983.

Norton, C. C., F. R. Mosher, B. Hinton, D. W. Martin, D. Santek, and W. Kuhlow, A model for calculating desert aerosol turbidity over oceans from geostationary satellite data, *J. Appl. Meteorol.*, *19*, 633–642, 1980.

Payne, R. E., Albedo of the sea surface, *J. Atmos. Sci.*, *29*, 959–960, 1972.

Rao, C. R. N., E. P. McClain, and L. L. Stowe, Remote-Sensing of aerosols over the oceans using AVHRR data theory, practice and applications, *Int. J. Remote Sens.*, *10*, 743–749, 1989.

Remer, L. A., S. Gasso, D. Hegg, Y. J. Kaufman, and B. N. Holben, Urban/industrial aerosol: Ground-based Sun/sky radiometer and airborne in situ measurements, *J. Geophys. Res.*, this issue.

Remer, L. A., Y. J. Kaufman, and B. N. Holben, The size distribution of ambient aerosol particles: Smoke versus urban/industrial aerosol, in *Global Biomass Burning*, edited by J. Levin, pp. 519–530, MIT Press, Cambridge, Mass., 1996.

Salomonson, V. V., W. L. Barnes, P. W. Maymon, H. E. Montgomery, and H. Ostrow, MODIS: Advanced facility instrument for studies of the Earth as a system, *IEEE Trans. Geosci. Remote Sens.*, *27*, 145–153, 1989.

Schubert, S., R. Rood, and J. Pfaendtner, An assimilated dataset for Earth science applications, *Bull. Am. Meteorol. Soc.*, *74*, 2331–2342, 1993.

Shettle, E. P., Optical and radiative properties of a desert aerosols model, in *IRS'84: Current Problems in Atmospheric Radiation*, edited by G. Fiocco, pp. 243, A. Deepak, Hampton, Va., 1984.

Shettle, E. P., and R. W. Fenn, Models for the aerosol of the lower atmosphere and the effect of humidity variations on their optical properties, *AFGL Tech. Rep.*, *AFGL-TR 790214*, Opt. Phys. Div., Air Force Geophys. Lab., Hanscom Air Force Base, Mass., 1979.

Tanré, D., C. Devaux, M. Herman, R. Santer and J. Y. Gac, Radiative properties of desert aerosols by optical ground-based measurements at solar wavelengths, *J. Geophys. Res.*, *83*, 14,223–14,231, 1988a.

Tanré, D., P. Y. Deschamps, C. Devaux, and M. Herman, Estimation of Saharan aerosol optical thickness from blurring effects in thematic mapper data, *J. Geophys. Res.*, *93*, 15,955–15,964, 1988b.

Tanré, D., M. Herman, Y. J. Kaufman, Information on the aerosol size distribution contained in the solar reflected spectral radiances, *J. Geophys. Res.*, *101*, 19,043–19,060, 1996.

Travis, L. D., EOSP: Earth Observing Scanning Polarimeter, in *EOS Reference Handbook 1993*, edited by G. Asrar and D. J. Dokken, pp. 74–75, NASA, 1993.

Van de Hulst, H. V., *Light Scattering by Small Particles*, John Wiley, New York, 1957.

Wang, M., and H. R. Gordon, Radiance reflected from the ocean-atmosphere system: Synthesis from individual components of the aerosols size distribution, *Appl. Opt.*, *33*, 7088–7095, 1994.

Wiscombe, W. J., and G. W. Grams, Backscattered fraction in two-stream approximations, *J. Atmos. Sci.*, *33*, 2440–2451, 1976.

Wiscombe, W. J., and A. Mugnai, Scattering from nonspherical Chebyshev particles, 2, Means of angular scattering patterns, *Appl. Opt.*, *27*, 2405–2421, 1988.

Whitby, K. Y., The physical characteristics of sulfur aerosols, *Atmos. Environ.*, *12*, 135–159, 1978.

Whitlock, C. H., D. S. Bartlett, and E. A. Gurganus, Sea foam reflectance and influence on optimum wavelength for remote sensing of ocean aerosols, *Geophys. Res. Lett.*, *9*, 719–722, 1982.

M. Herman and D. Tanré, Laboratoire d'Optique Atmosphérique, UA CNRS 713, U.S.T. de Lille, Bat. P5, 59655, Villeneuve d'Ascq, France.

Y. J. Kaufman, Laboratory for Atmospheres, NASA GSFC, Greenbelt, MD 20771.

S. Mattoo, Applied Research Corporation, Landover, MD 20785.

(Received March 19, 1996; revised October 30, 1996;
accepted October 30, 1996.)